Analysis and Design of Multichannel High-Frequency Wireless Power Transfer System Based on Load Impedance Compression

Zhan Sun, *Student Member, IEEE*, Yijie Wang, *Senior Member, IEEE*, Xianrui Zeng,
Yueshi Guan, *Senior Member, IEEE*, and Dianguo Xu, *Fellow, IEEE*

***Abstract*—Miniaturization is one of the main trends in the development of power supplies. High frequency helps to improve the flexibility of the magnetic field space of wireless power transfer technology, making it more suitable for multiload application scenarios. However, it will also increase the sensitivity of the system, causing mutual coupling problems in multiload designs. To this end, this article proposes a load impedance compression mechanism for wired/wireless dual-load applications, adding an impedance conversion network to adjust the branch impedance value. From the perspective of impedance trajectory, the influence of the change in coupling coefficient is compressed, the complex and intertwined trajectory curves between multiple loads are decoupled, and the independence of load power is restored. Meanwhile, based on the traditional secondary side design method, a coil and rectifier impedance trajectory constraint model under variable coupling coefficient is further proposed. Finally, the influence of different power amplifier output filtering conditions on the load branch is analyzed, and the overall design process is given.**

***Index Terms*—Impedance trajectory, load impedance compression, multiload applications, wireless power transfer (WPT).**

I. INTRODUCTION

Wireless power transfer (WPT) has become a research hotspot due to its high efficiency and convenience. Especially in multiload applications (such as, smart homes, industrial production, and medical equipment), WPT technology has opened up new ways to meet the simultaneous power supply requirements of different devices. Certainly, the different energy requirements and efficiency quotas of different loads also bring difficulties to the design of multiload systems, which is one of the main problems to be solved. To achieve high insulation charging of gate drivers in multilevel converters and enhance long-distance power transmission capabilities, a WPT system consisting of multiple wireless repeater unit structures was proposed, which can achieve independent power control and constant voltage output of multiple loads. Among them, each wireless repeater unit is composed of bipolar coils and placed vertically to eliminate the influence of cross-coupling [1]. Further, based on this article, an asymmetric coil structure was proposed to obtain equal load voltage distribution [2]. The *LCC* structure was also used to obtain load-independent current [3]. Moreover, it is feasible to use load coils to power multiple loads. This three-coil structure is easy to transmit power to multiple loads and has the advantages of compact structure and controllable power flow. In [4], uncoupled and coupled load coils were studied, and the equivalent reflected resistance was introduced to mathematically decouple the double load transmission model of the coupled load coil.

Another common method of wireless power supply for multiple loads is to use multifrequency technology. In [5], multiple half-bridge inverters share the same input power supply, generate multiple switching frequencies, drive synchronously and superimpose on the transmitter resonant circuit. The resonant frequency of the transmitter/receiver can be modulated in adjacent operating frequency regions to achieve efficient power distribution for multiple loads. Similarly, in [6], a dual-frequency multirelay dual-load WPT system with a shared input power supply was proposed to power online monitoring equipment of high-voltage transmission lines. At the receiving end, a parallel *LC* filter was used to reduce the cross-interference of nontarget frequencies to achieve selective power allocation (this method, i.e., adding an *LC* network, to suppress eddy current losses was also demonstrated in [7]). Modeling was performed based on the quadratic eigenvalues to optimize the operating frequency and obtain constant current output performance. Multifrequency energy can also be generated by a single inverter through multifrequency programmed pulse width modulation combined with harmonic elimination [8], thus achieving better tradeoffs in system size, complexity, power transfer capability, output regulation, etc. Furthermore, in order to improve the system power density, a three-phase high-frequency inverter with a triangular transmission circuit was proposed in [9]. By setting an equivalent transmission resonant circuit, three modes of single-frequency

---

Received 17 January 2025; revised 26 March 2025 and 12 May 2025; accepted 22 May 2025. Date of publication 29 May 2025; date of current version 5 August 2025. This work was supported in part by the National Natural Science Foundation of China under Grant 523B2082, in part by the Fundamental Research Funds for the Central Universities under Grant HIT.DZJJ.2023024, and in part by the National Natural Science Foundation of China under Grant 51922033. Recommended for publication by Associate Editor M. Ponce-Silva. *(Corresponding author: Yijie Wang.)*

The authors are with the School of Electrical Engineering and Automation, Harbin Institute of Technology, Harbin 150001, China (e-mail: 21b906030@stu.hit.edu.cn; wangyijie@hit.edu.cn; 20s006103@stu.hit.edu.cn; guanyueshi@hit.edu.cn; xudiang@hit.edu.cn).

Color versions of one or more figures in this article are available at https://doi.org/10.1109/TPEL.2025.3574807.

Digital Object Identifier 10.1109/TPEL.2025.3574807

transmission, concurrent frequency transmission and additional frequency transmission can be performed. Different resonant energies are transmitted to multiple loads, saving a large number of power devices. Similarly, in [10], a single-stage transmitter is formed by integrating a totem pole rectifier operating in discontinuous conduction mode and a full-bridge inverter with asymmetric voltage compensation control. This reduces the number of switching devices and is suitable for multiload wireless charging applications in consumer electronics. In [11], to meet both Qi and AirFuel standards, a high-power density dual-band transmitter and reconfigurable rectifier were proposed to adapt to the different charging requirements of the load.

Then, based on multifrequency operation, the multiphase structure of the transmitting coil can further enhance the misalignment tolerance [12]. At the same time, combined with the phase shift control method, stable output power can be achieved to meet the load misalignment requirements. Furthermore, it is worth noting that when multiple coils work under over-coupling conditions, frequency bifurcation will occur, thereby reducing the transfer efficiency. To address this problem, in [13], a method for simultaneous power transfer of multiple loads using frequency bifurcation was proposed, combined with automatic power flow control to estimate the load current, thereby facilitating the selection of load coils. From the control perspective, for multiload systems, in [14], directional energy transfer and rotational energy transfer methods were compared, and guidance on selecting the transfer method in different scenarios was given. In [15], a time-division multiplexing method is used to charge multiple loads, and the power allocation ratio of each load corresponds to the charging time ratio. From an application perspective, in [16], a transmitting coil based on direct and quadrature rotating magnetic fields was proposed to construct a six-degree-of-freedom omnidirectional wireless power supply environment, which is suitable for multiload Internet of Things systems. Interestingly, wireless multiload technology can also be used to achieve high-voltage and high-isolation power supply [17]. It adopted a double-sided *LCC* compensation topology, and multiple receiving ends were rectified separately and connected in series to generate high-voltage output. In order to obtain high power density, the inductive components were stacked and integrated. Decoupling and voltage balancing were achieved through compensation parameter design.

High frequency and miniaturization are among the mainstream trends in the development of power supplies nowadays [18]. However, this also makes the design of high-frequency multiload systems more difficult than traditional low-frequency systems [19], [20]. Especially after entering the industrial scientific and medical frequency band, such as 6.78 MHz, 13.56 MHz, etc. This is because at this time the system is no longer purely resistive conduction [21], [22] and needs to be comprehensively considered from the perspective of impedance compression [23], [24]. In [25], a 6.78 MHz scalable multireceiver WPT system was introduced, using the rectifier shunt capacitance and power amplifier (PA) output current as optimization parameters. Efficient power transfer to multiple loads was achieved within the expected cross-coupling range. Then another method to solve the high-frequency multiload cross-coupling was introduced in [26]. That is, from the perspective of circuit derivation, the decoupling effect is restored by adding the optimal load reactance, while retaining the consistency of the important external characteristics of the system. Multiple loads can freely join or leave, so the system needs to have the ability of automatic control and adaptive power allocation. To this end, a control method based on mathematical theory was adopted to transform the charging problem into a generalized Stackelberg game. By searching for Lagrange multipliers, the generalized Nash equilibrium between receivers was achieved [27]. Certainly, to simplify the complexity of the control algorithm, time division multiplexing is still feasible. Combined with the maximum efficiency point tracking, the overall efficiency of the system can be improved [28]. Another simplification, introduced in [29], built a single receiver model to replace the actual multiload case. Moreover, the unique balancing feature of high-frequency WPT can also be used in multibattery charging voltage balancing [30].

For the application of tightly coupled high-frequency wired branches, a system design method for a current-driven class E circuit was proposed [31]. Through theoretical analysis and numerical derivation, the phase of the input impedance and the stress of the diode are optimized to achieve the quasi-resistive characteristics of the input impedance, and hysteresis control is used to regulate the output voltage. In [32], a high-frequency system composed of a class Φ_2 inverter, a fully resonant class E rectifier, and a T-type matching network was studied. An accurate time-domain model is established, and a T-type network with the ability of inductance-resistance transformation is designed to ensure the soft-switching characteristics. In [33], high-frequency synchronous rectification control and parameter design methods were introduced. The soft switching of the MOSFET is achieved by adjusting the equivalent impedance, and a self-oscillating resonant gate drive scheme is proposed to reduce the losses. Moreover, based on the principle of zero phase difference, a matching network for a very high frequency (VHF) converter was designed, and a shared external drive circuit was proposed in [34]. The inverter and the rectifier are driven by the same oscillation signal to increase the duty cycle and reduce the conduction loss, which has the advantages of simple structure and accurate timing. In [35], from the perspective of the magnetic core design, by utilizing the characteristic of zero leakage inductance of the inner winding of the nested toroidal air-core transformer, the effect of zero phase difference is also achieved, the synchronous rectification control is simplified, and efficient synchronous rectification is realized at the megahertz level. The efficiency is increased by 6.8% compared with that of the traditional PCB transformer. Similarly, an MEMS toroidal air-core inductor embedded in silicon was developed [36]. By removing the silicon core, the quality factor and the operating frequency are improved. Experiments show that it has better performance in the VHF band, and the efficiency improvement is verified in a class E converter. In [37], an optimal duty cycle-assisted pulse frequency modulation control strategy was proposed. By dynamically calculating the optimal duty cycle at the switching frequency, zero voltage switching is ensured and the reverse conduction loss is minimized. This method models the rectifier as a reactance element controlled by frequency.

After simplifying the resonant network, the voltage at the switching node and the output power are derived. Combining on/off modulation, the load range is expanded. Experiments show that compared with the traditional frequency modulation control, the power loss is reduced by 35.9% at 40% load, while maintaining a continuous power flow and low output ripple. In [38], for bendable devices, a megahertz low-profile converter based on an air-core inductor was designed. A mathematical model and an inductance calculation method for the bendable planar spiral coil in different bending states are established. The T-type matching network is optimized to achieve a weakly inductive equivalent input impedance, ensuring the soft-switching characteristics and high efficiency within the full bending range. The system efficiency is increased by 4% compared with the traditional method. A resonant push-pull dc converter was developed [39].

Its design does not require multiresonant tuning and can provide a constant current within a wide output voltage range during unregulated operation. A normalized design criterion is established based on the steady-state analytical solution, and it has the characteristic of fast transient response, simplifying the design process of the converter. In [40], coupled inductors were introduced into a class-E parallel resonant inverter. By optimizing the turns ratio, the maximum power is increased while maintaining a duty cycle of 0.5 and soft switching. Equivalent circuit analysis shows that in the load resistance range of 40:1, the voltage stress variation of this design is less than 15%, and the secondary circuit compensation design is simplified. In [41], an integrated class-Φ_2 converter was proposed. By utilizing the branching phenomenon of the impedance matching network of the isolation transformer, the additional *LC* branch of the traditional class-Φ_2 converter is omitted. A quasi-square wave voltage waveform is realized through multiharmonic tuning (fundamental frequency, second and third harmonics), reducing the circuit complexity, and a mathematical model is established to analyze the frequency response in the branching state. In [42], an innovative integration method for high-frequency air-core transformers was proposed. The transformer is directly embedded in a multilayer PCB. The structure is optimized through finite element analysis, reducing the floor area by 46% and the parasitic inductance by 64%. This design ensures that the magnetic field of the internal transformer does not interfere with the top-layer components, and at the same time, a highly consistent manufacturing process is achieved, significantly improving the power density.

In this article, a study is conducted on the high-frequency 6.78 MHz wired/wireless dual-load system. Here, the wired load branch provides stable power transmission for devices with relatively fixed positions, and the wireless load branch allows the load devices to move freely within a certain range, improving the charging convenience of users, as shown in Fig. 1. The load impedance compression principle is innovatively proposed to simplify the design difficulty of the high-frequency system.

This rest of this article is organized as follows. In Section II, the design difficulties of traditional high-frequency systems facing multiple loads are introduced. In Section III, the principle of the proposed load impedance compression is given. Section IV analyzes the PA design. Section V is the experimental verification. Section VI discusses the expansion of future research. Finally, Section VII concludes this article.

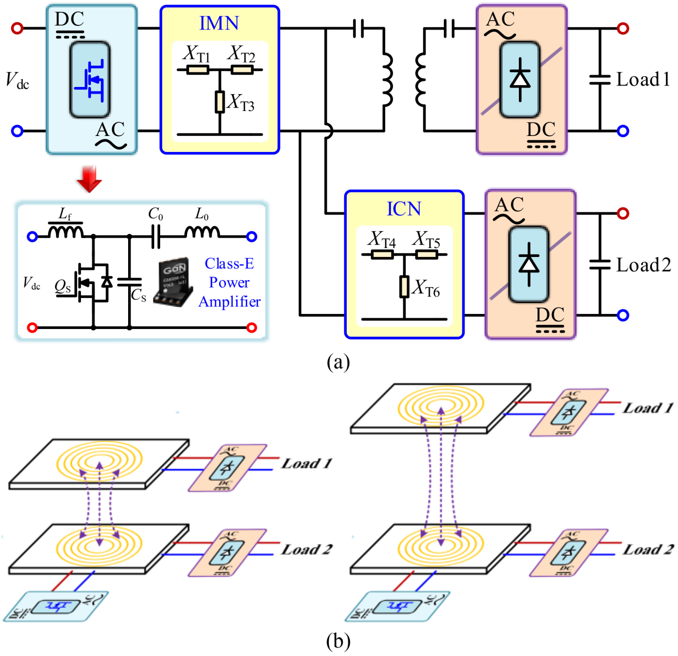

(a)

(b)

Fig. 1. Technology application. (a) Wired/wireless dual load high frequency 6.78 MHz system. (b) Application schematic.

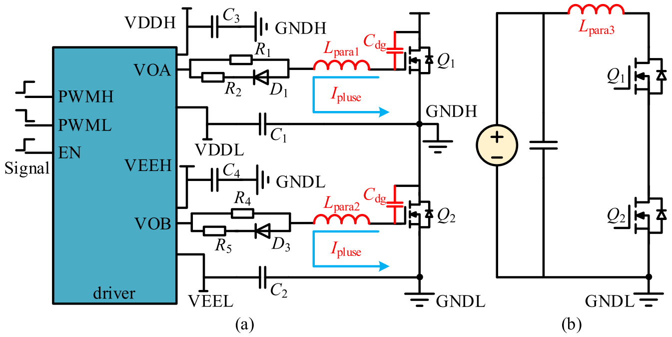

(a) (b)

Fig. 2. High frequency class-D circuit. (a) Drive circuit. (b) Power circuit.

II. Analysis of the Structure of Traditional Multiload High-Frequency WPT System

Regarding the selection of high-frequency PA, the common ones include bridge structure and resonant class-E circuit. The bridge structure is relatively robust, but it corresponds to high harmonic content. At the same time, the floating drive causes pulse current in the drive circuit due to the high-frequency parasitic inductance, which will cause the peak of the drive signal, as shown in Fig. 2(a). The power circuit will also cause oscillation on the rising edge due to the line inductance, as shown in Fig. 2(b). Therefore, this article selects the Class-E circuit, which is more efficient, more commonly used but more sensitive, as the PA. After entering the industrial scientific medical band, the rectifier input voltage and current no longer present a zero-phase

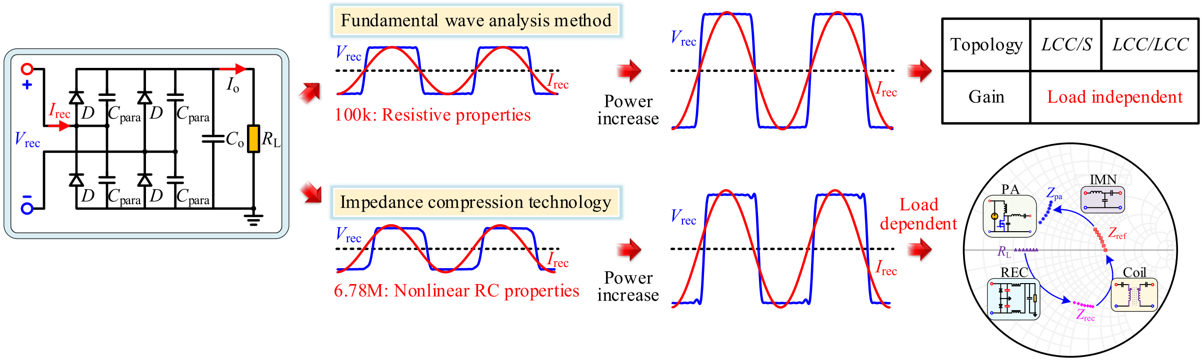

Fig. 3. Performance comparison of 100 kHz and 6.78 MHz rectifiers.

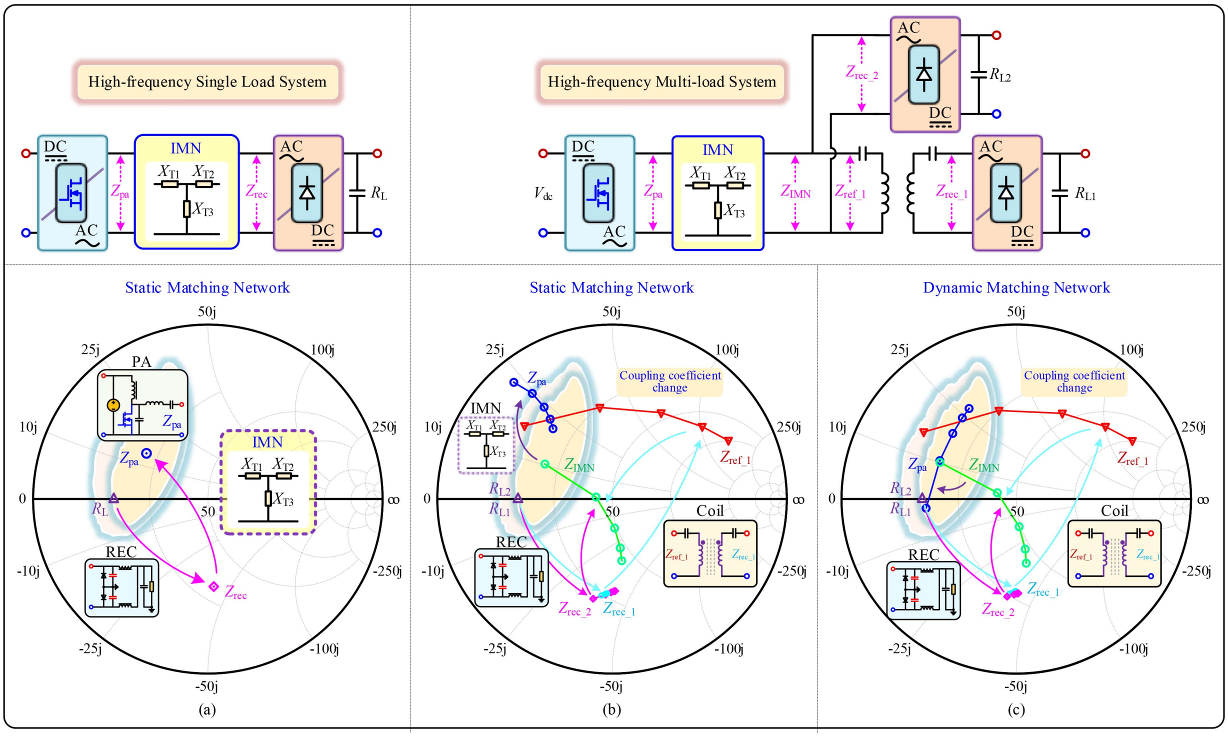

Fig. 4. High frequency system impedance trajectory changes. (a) Single-point impedance compression design for wired load systems. (b) Impedance compression design for high frequency wired/wireless dual load systems. (c) Impedance compression design of high-frequency wired/wireless dual-load system based on PA efficiency optimization.

angle, as shown in Fig. 3. Due to the increased proportion of the parasitic capacitance effect, the input current exceeds the voltage at this time. The rectifier exhibits a capacitive impedance characteristic that varies nonlinearly with power [43]

$$R_{\mathrm{rec\_FBR}} = \frac{4R\left[\cos\left(2\theta\right)+1\right]}{\left(1+\tan^2\theta\right)\pi^2\cos\theta},$$

$$X_{\mathrm{rec\_FBR}} = -\frac{4R\left[\cos\left(2\theta\right)+1\right]\tan\theta}{\left(1+\tan^2\theta\right)\pi^2\cos\theta} \qquad (1)$$

$$\theta = \sqrt{\frac{4RQ_j}{4RQ_j+2\pi V_o/\omega}} \qquad (2)$$

where Q_j is the junction charge stored at the diode junction cap. $R_{\mathrm{rec\_FBR}}$ and $X_{\mathrm{rec\_FBR}}$ represent the real and imaginary input impedance of the full-bridge rectifier. R and V_o correspond to the rectifier output load and voltage, respectively. In low-frequency systems, the load-independent characteristics of *LCC/S* or bilateral *LCC* derived by the classic fundamental analysis method will change in high-frequency systems. Therefore, in this article, the trajectory analysis will be conducted from the perspective of impedance compression, which is more accurate. Fig. 4 shows the impedance trajectory changes of the single wired load system and the wired/wireless dual load system under the traditional impedance compression design. Fig. 5 shows the output performance of the class-E PA used in the analysis of Fig. 4. The yellow area is the high-efficiency impedance range of the PA, where the

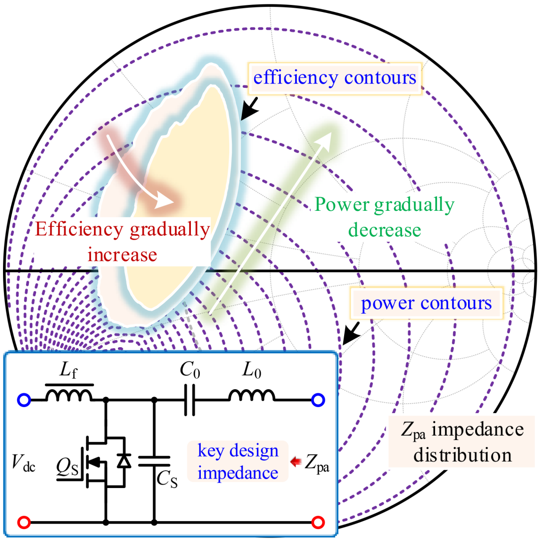

Fig. 5. Class-E PA output performance based on Z_{pa} impedance variation.

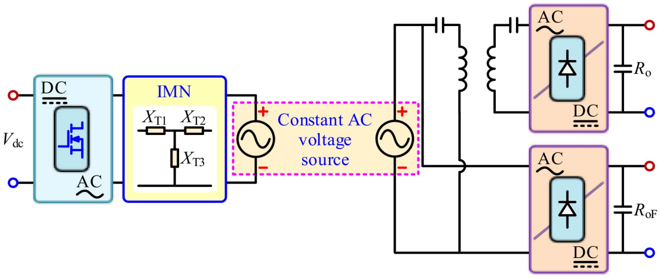

Fig. 6. Intermediate constant voltage AC bus structure.

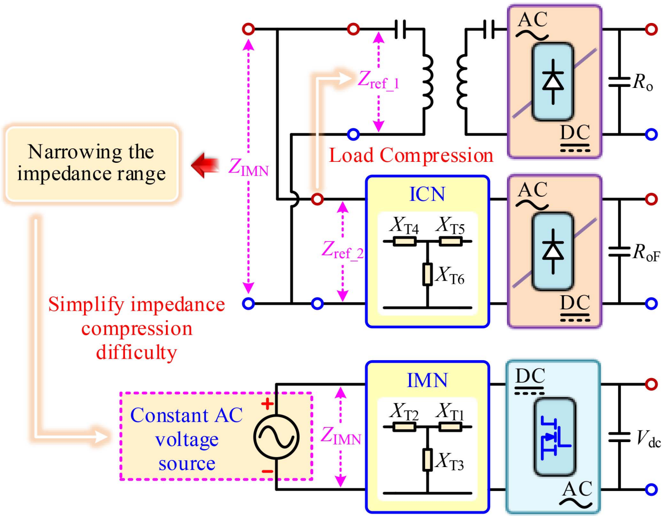

Fig. 7. Load impedance compression concept.

load-pull scan is performed with the PA output impedance Z_{pa}. As the red line points, the PA efficiency increases as it moves toward the center. The purple curve is the PA power output contour line, and as the green arrow points, the power output gradually decreases. Then, for the case of a single wired load, the load resistance R_L presents a capacitive input impedance Z_{rec} through the rectifier, as shown in Fig. 4(a). Obviously, Z_{rec} is not in the high efficiency range of the PA. Therefore, an impedance compression network (IMN) is added to convert Z_{rec} to Z_{pa}. This satisfies the high efficiency operation of the PA while adjusting and guarantying the power level required by the system. However, when the number of loads begins to increase, as shown in Fig. 4(b), the impedance trajectory begins to become complicated. Similarly, loads R_{L1} and R_{L2} (purple triangles) are capacitive after passing through the rectifier. The wireless branch needs to be able to move freely, so $Z_{\mathrm{rec\_1}}$ (cyan circle) is coupled by the coil to obtain the reflected impedance $Z_{\mathrm{ref\_1}}$ (red triangle) under the change of the coupling coefficient. It can be seen that the impedance variation range of $Z_{\mathrm{ref\_1}}$ is relatively wide. This will cause the synthetic impedance Z_{IMN} (green circle) to vary widely. Then, under the same impedance compression design, Z_{pa} may not be able to maintain efficient operation. Certainly, some dynamic IMN [44], [45], [46], [47] can be used to reoptimize the impedance trajectory to ensure that Z_{pa} falls into the high-efficiency range, as shown in Fig. 4(c). However, it will increase the complexity of the system. More importantly, the impedance trajectory of the system is still relatively chaotic, the power distribution of each load cannot be accurately obtained. There is power coupling between loads, and the independent characteristics of each load are not achieved. In this way, the requirements of load scalability cannot be further met.

III. ANALYSIS AND DESIGN OF LOAD IMPEDANCE COMPRESSION MECHANISM

To address the problem of chaotic impedance trajectories of multiple loads under traditional impedance compression design, this article proposes a load impedance compression mechanism. The initial idea is to construct an intermediate constant voltage ac bus and distribute the complex impedance trajectory design into two parts to solve it, as shown in Fig. 6. In this way, compared with the PA directly outputting power that is difficult to determine, it is actually easier for the load to estimate the power obtained through the secondary bus. Therefore, in order to make PA output constant voltage, it is necessary to greatly compress the synthetic impedance Z_{IMN}, so as to facilitate the impedance trajectory design of Z_{PA}. After all, the impedance compression capability of static IMN is limited. Then, the design idea of load impedance compression is naturally born, as shown in Fig. 7. That is, by connecting the load branch reflection impedance $Z_{\mathrm{ref\_1}}$ and $Z_{\mathrm{ref\_2}}$ in parallel, the synthetic impedance Z_{IMN} can be reduced. Generally, the reflected impedance of the wireless load branch is affected by the change of the coupling coefficient, and the variation range of $Z_{\mathrm{ref\_1}}$ is relatively wide. Therefore, adding an impedance conversion network (ICN) to the wired branch can not only adjust the reflected impedance $Z_{\mathrm{ref\_2}}$, but also be used to achieve fixed power transmission of the wired branch. Fig. 8 shows the post-stage circuit structure used in this article. The full-wave rectifier is selected because it is more commonly used and can provide better real impedance.

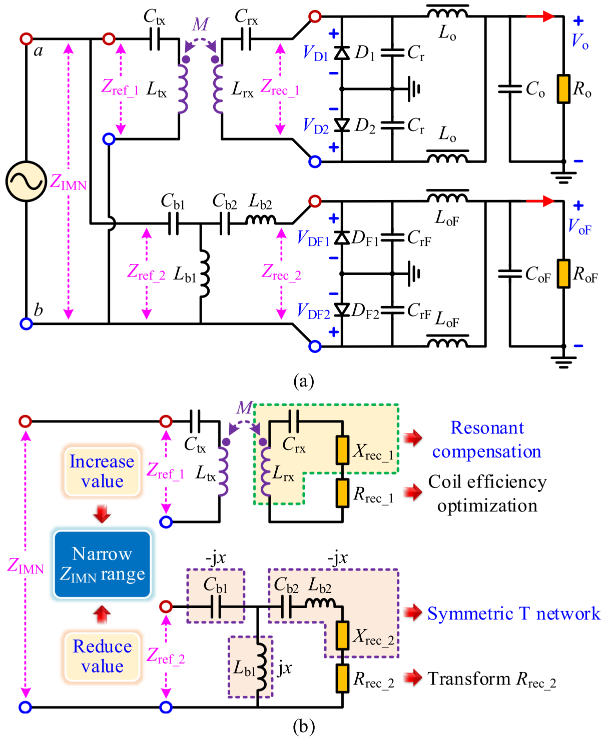

Fig. 8. Post-stage circuit structure. (a) Complete Circuit. (b) Simplified Circuit.

Then, the next step is to derive the formula. First, the rectifier input impedance is equal to:

$$\begin{cases} Z_{\mathrm{rec\_1}} = R_{\mathrm{rec\_1}} + jX_{\mathrm{rec\_1}} \\ Z_{\mathrm{rec\_2}} = R_{\mathrm{rec\_2}} + jX_{\mathrm{rec\_2}} \end{cases} \tag{3}$$

where R_{rec} and X_{rec} represent the real and imaginary components of the full-wave rectifier input impedance, respectively, [22]

$$\begin{aligned} R_{\mathrm{rec}} = \frac{2\sin(\phi_{\mathrm{rec}} + 2\pi D)}{\pi\omega C_r} \Bigg[& \sin(\phi_{\mathrm{rec}} + 2\pi D) - \sin\phi_{\mathrm{rec}} \\ & + 2\pi(1-D)\cos\phi_{\mathrm{rec}} \\ & + \frac{\cos\phi_{\mathrm{rec}} - \cos(\phi_{\mathrm{rec}} + 2\pi D)}{4\sin(\phi_{\mathrm{rec}} + 2\pi D)} \\ & + \frac{\cos 2(\phi_{\mathrm{rec}} + 2\pi D) - \cos 2\phi_{\mathrm{rec}}}{\tan(\phi_{\mathrm{rec}} + 2\pi D)} \Bigg] \end{aligned} \tag{4}$$

$$\begin{aligned} X_{\mathrm{rec}} = -\frac{2\sin(\phi_{\mathrm{rec}} + 2\pi D)}{\pi\omega C_r} \Bigg[& \cos\phi_{\mathrm{rec}} + 2\pi(1-D)\sin\phi_{\mathrm{rec}} \\ & - \frac{\sin\phi_{\mathrm{rec}}}{\tan(\phi_{\mathrm{rec}} + 2\pi D)} - \frac{\cos(\phi_{\mathrm{rec}} + 2\pi D)}{2} \\ & + \frac{2\pi(1-D) + \sin\phi_{\mathrm{rec}}\cos\phi_{\mathrm{rec}}}{2\sin(\phi_{\mathrm{rec}} + 2\pi D)} \Bigg] \end{aligned} \tag{5}$$

$$\begin{aligned} C = \frac{1}{\omega R} \Bigg[& \frac{1}{4\pi} - \frac{\pi}{2}(1-D)^2 \\ & + \frac{2\pi(1-D)\cos(\phi_{\mathrm{rec}} + 2\pi D) - \sin\phi_{\mathrm{rec}}}{4\pi\sin(\phi_{\mathrm{rec}} + 2\pi D)} \Bigg] \end{aligned} \tag{6}$$

$$\tan\phi_{\mathrm{rec}} = -\frac{\pi(1-D)\sin(2\pi D) + \sin^2(\pi D)}{\pi(1-D)\cos(2\pi D) + \sin(\pi D)\cos(\pi D)}. \tag{7}$$

Here, D is the duty cycle of the diode, and ϕ_{rec} is the initial phase. In simple terms, it can also be considered as a nonlinear changing function of load, power and parallel capacitance

$$\begin{cases} R_{\mathrm{rec}} = f_1(P, C_r, R) \\ X_{\mathrm{rec}} = f_2(P, C_r, R) \end{cases}. \tag{8}$$

For the wireless branch, it is necessary to compensate the reactive component of the secondary side as much as possible to improve the coil efficiency, that is

$$\mathrm{Imag}\{Z_{S1}\} = j\omega L_{rx} + \frac{1}{j\omega C_{rx}} + jX_{\mathrm{rec\_1}} \approx 0. \tag{9}$$

However, as described in (8), when the output power of the wireless branch changes, its corresponding $X_{\mathrm{rec\_1}}$ will also change. Therefore, the above formula cannot guarantee that the secondary side is fully compensated under all coupling coefficients. The primary side compensation has no effect and can perform traditional full compensation

$$j\omega L_{tx} + \frac{1}{j\omega C_{tx}} = 0. \tag{10}$$

At this time, the reflected impedance $Z_{\mathrm{ref\_1}}$ is

$$\begin{aligned} Z_{\mathrm{ref\_1}} = & j\omega L_{tx} + \frac{1}{j\omega C_{tx}} + r_{tx} \\ & + \frac{\omega^2 M^2}{j\omega L_{rx} + \frac{1}{j\omega C_{rx}} + jX_{\mathrm{rec\_1}} + r_{rx} + R_{\mathrm{rec\_1}}}. \end{aligned} \tag{11}$$

Then, the coil efficiency can be expressed as

In traditional methods, only the efficiency analysis of the coil in the fully resonant state is usually considered. In this case, the coil efficiency can be simplified to

$$\eta_{\mathrm{coil\_simp}} = \frac{\omega^2 M^2 R_{\mathrm{rec\_1}}}{\omega^2 M^2 (R_{\mathrm{rec\_1}} + r_{rx}) + r_{tx}(R_{\mathrm{rec\_1}} + r_{rx})^2}. \tag{13}$$

Then, the efficiency peak is derived

$$\eta_{\mathrm{coil\_peak}} = \frac{\sqrt{{r_{rx}}^2 + \frac{\omega^2 M^2 r_{rx}}{r_{tx}}} - r_{rx}}{\sqrt{{r_{rx}}^2 + \frac{\omega^2 M^2 r_{rx}}{r_{tx}}} + r_{rx}}. \tag{14}$$

At this time, the real impedance of the rectifier corresponding to the peak value of the coil efficiency is

$$R^*_{\mathrm{rec\_1}} = \sqrt{{r_{rx}}^2 + \frac{\omega^2 M^2 r_{rx}}{r_{tx}}}. \tag{15}$$

Equation (15) is often used as the basis for the design of wireless branch rectifier parameters. At the maximum power point, the real part of the rectifier input impedance is set equal to $R*$ rec_1. However, in this article, since the wireless branch cannot be fully compensated in all misalignment situations, a new

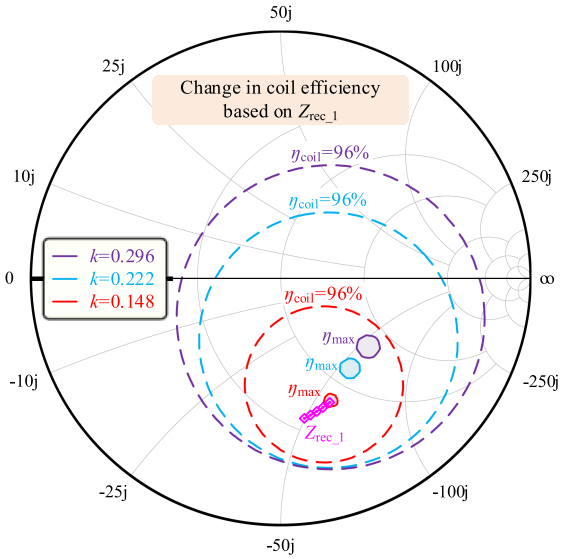

Fig. 9. Coil efficiency analysis based on impedance trajectory.

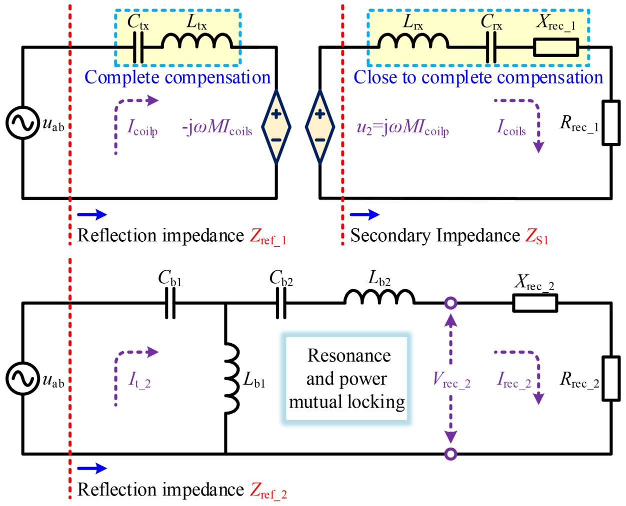

Fig. 10. Impedance equivalence analysis.

design method is required from the perspective of impedance trajectory. Likewise, the load-pull function of the advanced design system software is used. Here, the rectifier input impedance $Z_{\text{rec\_1}}$ is used as the base to depict the high efficiency impedance range of the coil under different coupling coefficients (k), as shown in Fig. 9.

From (12) shown at the bottom of this page to (14), it can be seen that the increase in mutual inductance (M) helps to improve the efficiency of the coil. Therefore, the minimum coupling coefficient is first selected for full compensation, and the rectifier parallel capacitor is designed to achieve the coil's maximum efficiency under this coupling coefficient. Then, by analyzing and calculating the $Z_{\text{rec\_1}}$ value under different coupling coefficients, the pink diamond impedance trajectory in Fig. 9 can be obtained. Finally, the $Z_{\text{rec\_1}}$ trajectory is compared to see whether it is within the high efficiency range of the coil under different coupling coefficients, so as to further adjust the rectifier parallel capacitance C_r value. Therefore, the selection of C_r is relatively flexible for wireless branches.

Then for the wired load branch, the design idea is mainly to reduce the reflected impedance $Z_{\text{ref\_2}}$ through ICN. First, according to Kirchhoff's voltage/current law (see Fig. 10)

$$\begin{bmatrix} u_{ab} \\ u_{ab} \\ V_{\text{rec\_2}} \end{bmatrix} = \begin{bmatrix} \frac{1}{j\omega C_{b1}} + j\omega L_{b1} & -j\omega L_{b1} & 0 \\ \frac{1}{j\omega C_{b1}} & \frac{1}{j\omega C_{b2}} + j\omega L_{b2} & V_{\text{rec\_2}} \\ 0 & R_{\text{rec\_2}} + jX_{\text{rec\_2}} & 0 \end{bmatrix} \begin{bmatrix} I_{\text{t\_2}} \\ I_{\text{rec\_2}} \\ 1 \end{bmatrix}. \tag{16}$$

Here, u_{ab} is the sinusoidal voltage source generated by PA through IMN. Further derivation

$$\begin{cases} I_{\text{rec\_2}} = \frac{j\omega L_{b1} * u_{ab}}{a + \frac{X_{\text{rec\_2}}}{\omega C_{b1}} - X_{\text{rec\_2}}\omega L_{b1} + j\omega L_{b1} R_{\text{rec\_2}} + \frac{R_{\text{rec\_2}}}{j\omega C_{b1}}} \\ Z_{\text{ref\_2}} = \frac{a + \frac{X_{\text{rec\_2}}}{\omega C_{b1}} - X_{\text{rec\_2}}\omega L_{b1} + j\omega L_{b1} R_{\text{rec\_2}} + \frac{R_{\text{rec\_2}}}{j\omega C_{b1}}}{R_{\text{rec\_2}} + jX_{\text{rec\_2}} + j\omega C_{b1} + j\omega L_{b2} + \frac{1}{j\omega C_{b2}}} \\ a = \frac{\omega^2 C_{b2} L_{b1} + \omega^2 C_{b2} L_{b2} + \omega^2 C_{b1} L_{b1} - \omega^4 L_{b1} L_{b2} C_{b1} C_{b2} - 1}{\omega^2 C_{b1} C_{b2}} \end{cases}. \tag{17}$$

At this time, let the resonant element satisfy the following equation:

$$\begin{cases} \frac{1}{j\omega C_{b1}} + j\omega L_{b1} = 0 \\ \frac{1}{j\omega C_{b2}} + j\omega L_{b2} + jX_{\text{rec\_2}} - \frac{1}{j\omega C_{b1}} = 0 \end{cases}. \tag{18}$$

Then, the simplified result can be obtained

$$\begin{cases} Z_{\text{ref\_2}} = \frac{1}{\omega^2 C_{b1}^2 R_{\text{rec\_2}}} \\ P_{oF} = \frac{u_{ab}^2 \omega^2 C_{b1}^2 R_{\text{rec\_2}}}{2} \end{cases}. \tag{19}$$

When the u_{ab} stable voltage is generated, the wired load power P_{oF} will be kept constant, thereby further maintaining the invariance of $Z_{\text{rec\_2}}$ [see (8)]. Based on this, (18) and (19) are guaranteed to be established, which is actually a state interlocking process. Fig. 11 shows the changes in the input impedance

---

$$\eta_{\text{coil}} = \frac{(R_{\text{rec\_1}} + r_{rx})}{r_{tx}(R_{\text{rec\_1}} + r_{rx})^2 + r_{tx}\left(\omega L_{rx} - \frac{1}{\omega C_{rx}} + X_{\text{rec\_1}}\right)^2 + \omega^2 M^2 (R_{\text{rec\_1}} + r_{rx})}$$

$$\times \frac{\omega^2 M^2 R_{\text{rec\_1}}}{R_{\text{rec\_1}} + r_{rx}} = \frac{\text{Re}\left\{Z_{\text{rec\_1}}\right\}}{\text{Re}\left\{Z_{\text{rec\_1}}\right\} + r_{rx}} \times \frac{\text{Re}\left\{\frac{\omega^2 M^2}{j\omega L_{rx} + \frac{1}{j\omega C_{rx}} + Z_{\text{rec\_1}} + r_{rx}}\right\}}{\text{Re}\left\{\frac{\omega^2 M^2}{j\omega L_{rx} + \frac{1}{j\omega C_{rx}} + Z_{\text{rec\_1}} + r_{rx}}\right\} + r_{tx}}. \tag{12}$$

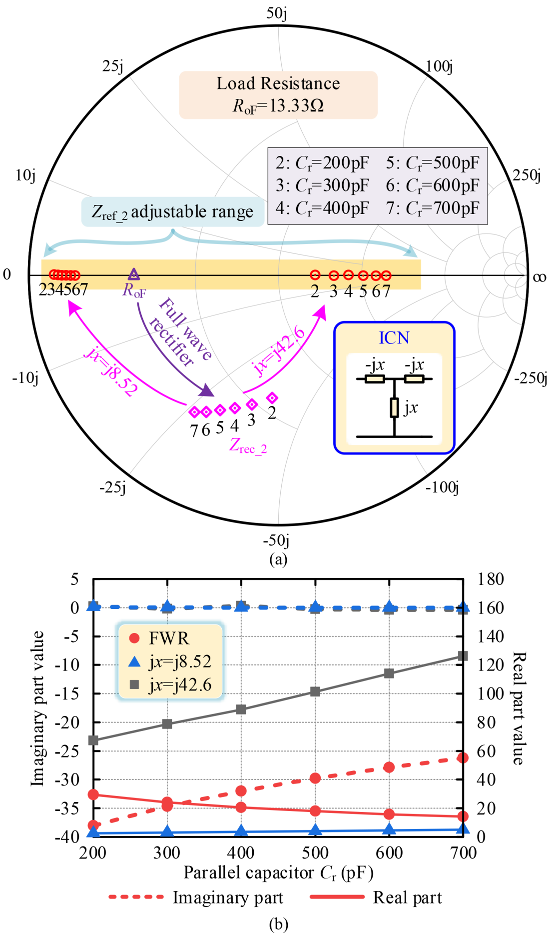

(a)

(b)

Fig. 11. Changes in wired branch impedance under different C_r and ICN values. (a) $Z_{\text{rec\_2}}$ and $Z_{\text{ref\_2}}$ impedance trajectories. (b) $Z_{\text{rec\_2}}$ and $Z_{\text{ref\_2}}$ impedance values.

$Z_{\text{rec\_2}}$ and reflected impedance $Z_{\text{ref\_2}}$ of the wired branch rectifier under different C_r and ICN resonance values. It can be seen that the reflected impedance eliminates the reactive component and can move left and right on the zero imaginary impedance horizontal axis, which has strong parameter flexibility. In order to reduce the variation range of the synthetic impedance Z_{IMN}, it is necessary to make $Z_{\text{ref\_2}}$ approach to the left on the horizontal axis. But on the other hand, the value of $Z_{\text{ref\_2}}$ should not be too small, which will increase the branch current I_{t_2} and generate additional losses. Ignoring the internal resistance of the line, Z_{IMN} is equal to

$$Z_{\text{IMN}} = \frac{\omega^2 M^2}{\omega^4 M^2 C_{b1}^2 R_{\text{rec\_2}} + j\omega L_{rx} + \frac{1}{j\omega C_{rx}} + jX_{\text{rec\_1}} + R_{\text{rec\_1}}}. \tag{20}$$

Fig. 12 shows the final impedance trajectory change of the wireless/wired dual-load high-frequency system and its corresponding impedance parameters. It can be seen that the wide reflection impedance $Z_{\text{ref\_1}}$ caused by the coupling change achieves a very small change range of Z_{IMN} under the impedance compression of the appropriate $Z_{\text{ref\_2}}$. The real part of Z_{IMN} changes by only 7.25 Ω. The three impedance trajectories are basically maintained near the zero imaginary impedance horizontal axis, reducing the reactive loss of the system.

IV. ANALYSIS AND DESIGN OF PA OUTPUT CONSTANT AC VOLTAGE SOURCE

The extreme compression of Z_{IMN} will greatly reduce the design difficulty of IMN and facilitate the impedance trajectory planning of Z_{pa}. IMN is placed after the classic class-E PA to play the role of impedance compression. According to Fig. 13, the PA output impedance Z_{pa} is further derived

$$Z_{pa} = \frac{Z_{\text{IMN}} jX_{T3} + Z_{\text{IMN}} jX_{T1} - X_{T2}X_{T3} - X_{T1}X_{T2} - X_{T1}X_{T3}}{Z_{\text{IMN}} + jX_{T2} + jX_{T3}}. \tag{21}$$

At this point, the three parameter degrees of freedom (X_{T1}-X_{T3}) of IMN need to be adjusted. While making the Z_{pa} impedance trajectory fall into the PA's high-efficiency range, its power transfer direction should satisfy the relationship between constant voltage output and load. That is, as the load increases, the power obtained should decrease, so as to keep the voltage constant.

Under such constraints, Fig. 14 shows the trajectory of Z_{pa}. The real impedance changes very little, and the imaginary part needs to satisfy

$$\frac{df\left\{\text{Imag}\left(\frac{Z_{\text{IMN}} jX_{T3} + Z_{\text{IMN}} jX_{T1} - X_{T2}X_{T3} - X_{T1}X_{T2} - X_{T1}X_{T3}}{Z_{\text{IMN}} + jX_{T2} + jX_{T3}}\right)\right\}}{dM} > 0. \tag{22}$$

Furthermore, it is worth noting that the output filtering effect of the PA will also affect the performance of the u_{ab}, as shown in Fig. 15. It can be seen that as the filtering capability is improved, the sinusoidal degree of u_{ab} becomes higher, and the asymmetry problem of the wired load branch becomes smaller. For the wireless load branch, due to the further filtering of the coupling coil matching, there is no voltage asymmetry in this branch. Certainly, the filtering network also needs to consider the power supply volume and loss. After several simulations and trade-offs, a relatively suitable set of parameter values can be obtained. Under this tradeoff, u_{ab} is not a completely sinusoidal waveform (after all, the filter network cannot be ideal), but in fact it does not affect the proposed impedance trajectory design method and system output performance. The overall process of the proposed design approach is summarized, as shown in Fig. 16.

V. EXPERIMENTAL VERIFICATION

To verify the correctness of the proposed theory, an experimental prototype was built, as shown in Fig. 17. Two electronic loads were used to simulate the R_o and R_{oF} of the system respectively. Fig. 18 shows the overall circuit structure of the dual-load branch high-frequency system. In Table I, the specific

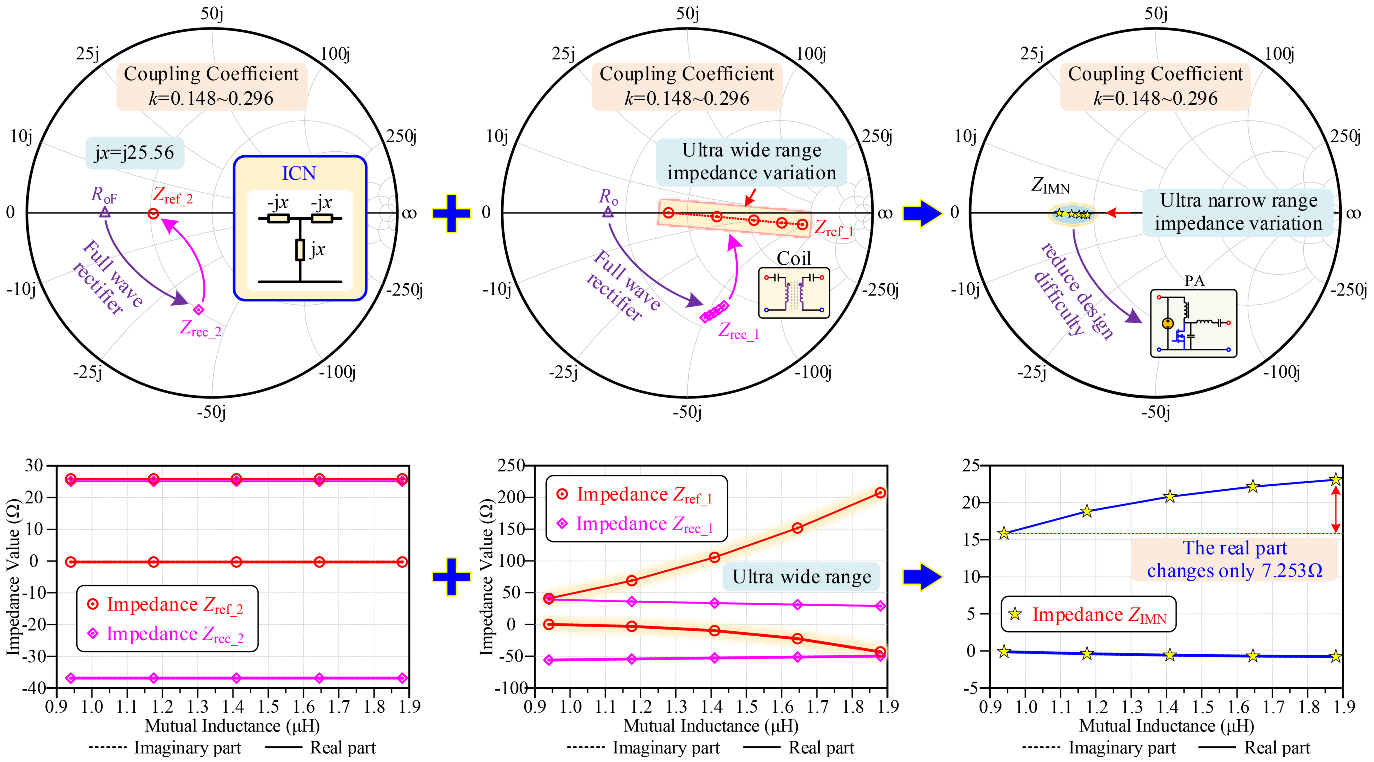

Fig. 12. Impedance trajectory changes of wireless/wired dual-load high-frequency system.

TABLE I
DUAL-LOAD WPT SYSTEM CIRCUIT PARAMETERS

	L_F	C_S	C_0	L_T	L_{T2}	C_T	C_{b1}	L_{b1}	C_{b2}	L_{b2}	C_{tx}	L_{tx},L_{rx}	r_{tx},r_{rx}	C_{rx}	C_r	C_{rF}	L_o	R_o	R_{oF}
Value	15	200	130	5.08	0.7	2	918.4	0.6	918.4	0.868	86.78	6.35	0.575	109.5	130	250	15	20	13.33
Unit	μH	pF	pF	μH	μH	nF	pF	μH	pF	μH	pF	μH	Ω	pF	pF	pF	μH	Ω	Ω

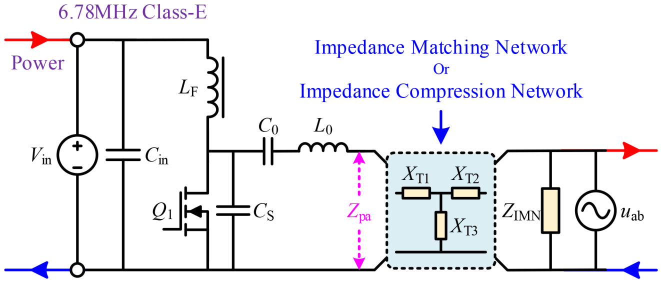

Fig. 13. PA outputs constant voltage source u_{ab}.

parameter values of each component are given. Here, the PA filter network (L_0) can also be integrated with X_{T1} (L_{T1}) in the IMN to further reduce the device size. For high-frequency systems, the actual circuit production and debugging should be more cautious than low-frequency kHz systems. For example, during the drawing of the hardware circuit board, great attention should be paid to avoid the two different networks from being directly opposite to each other, so as to avoid the generation of additional parasitic capacitance. After all, the normal capacitance value used in high-frequency systems is already at the pF level. At the same time, since most high-frequency systems use hollow coils to make resonant inductors, the inductors should be processed in the direction of orthogonal magnetic fields, and

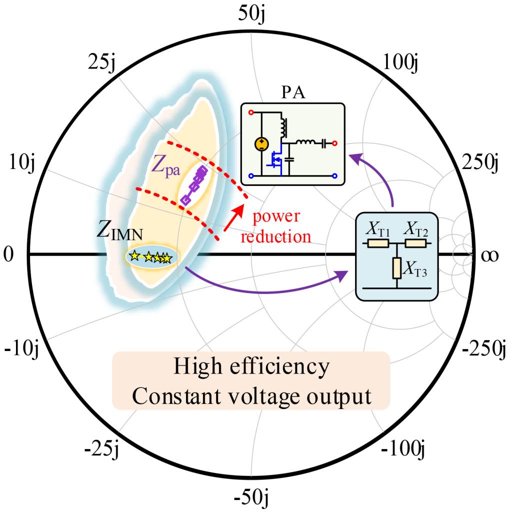

Fig. 14. Z_{pa} impedance trajectory design.

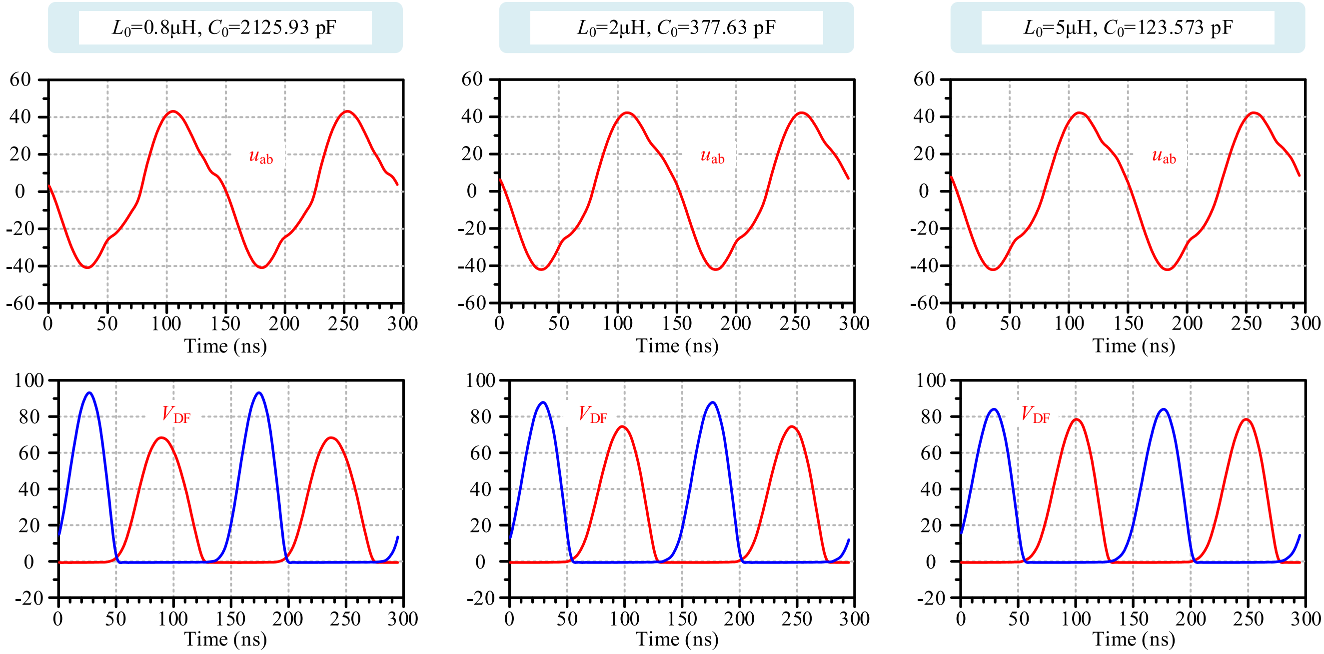

Fig. 15. PA output performance and wired branch rectifier voltage simulation waveform under different series filtering conditions.

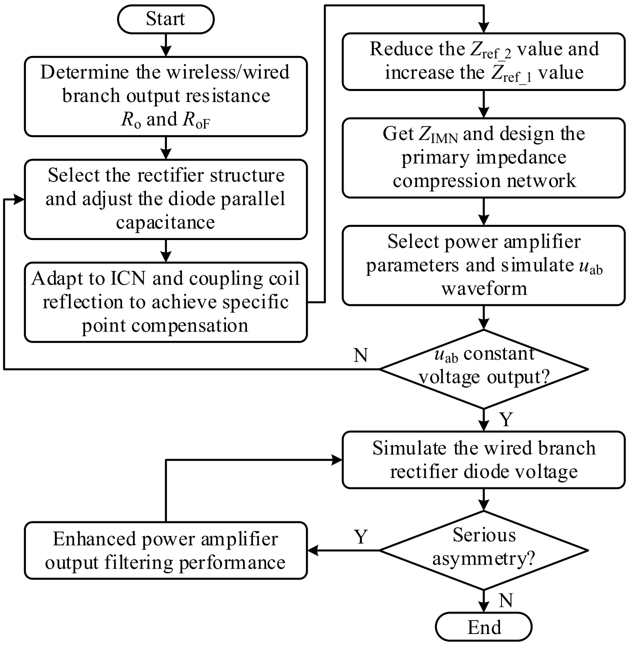

Fig. 16. Design flow chart of the proposed method.

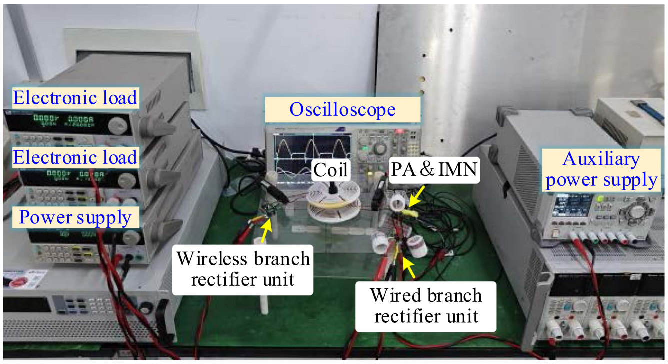

Fig. 17. Experimental prototype.

sufficient distance should be left to avoid unnecessary coupling between inductor components. For parameter determination, it is necessary to combine a high-precision and high-bandwidth impedance network analyzer to perform multiple measurements and take the average value to reduce device errors. Finally, it is necessary to re-correct each parameter according to different circuit boards and actual welding components in combination with circuit simulation to obtain results close to the theory.

Then in terms of experimental results, when the mutual inductance changes from 1.157 to 1.796 μH, the wired branch load always outputs 30 W and maintains the voltage at about 20 V, as shown in Figs. 19(c)–21(c). Although there is a certain asymmetry of the rectifier waveform, it is still within an acceptable range. From a certain perspective, this is also one of the unique operating states of such a wired/wireless dual-load high-frequency system. As for the wireless load branch, as analyzed above, due to the secondary filtering effect of the coil matching, the rectifier waveform of this part is not affected by harmonics and maintains good symmetry. As the mutual inductance decreases, its power output capacity gradually increases. Fig. 19 corresponds to the situation where the system has an overall output of 33.87 W, and

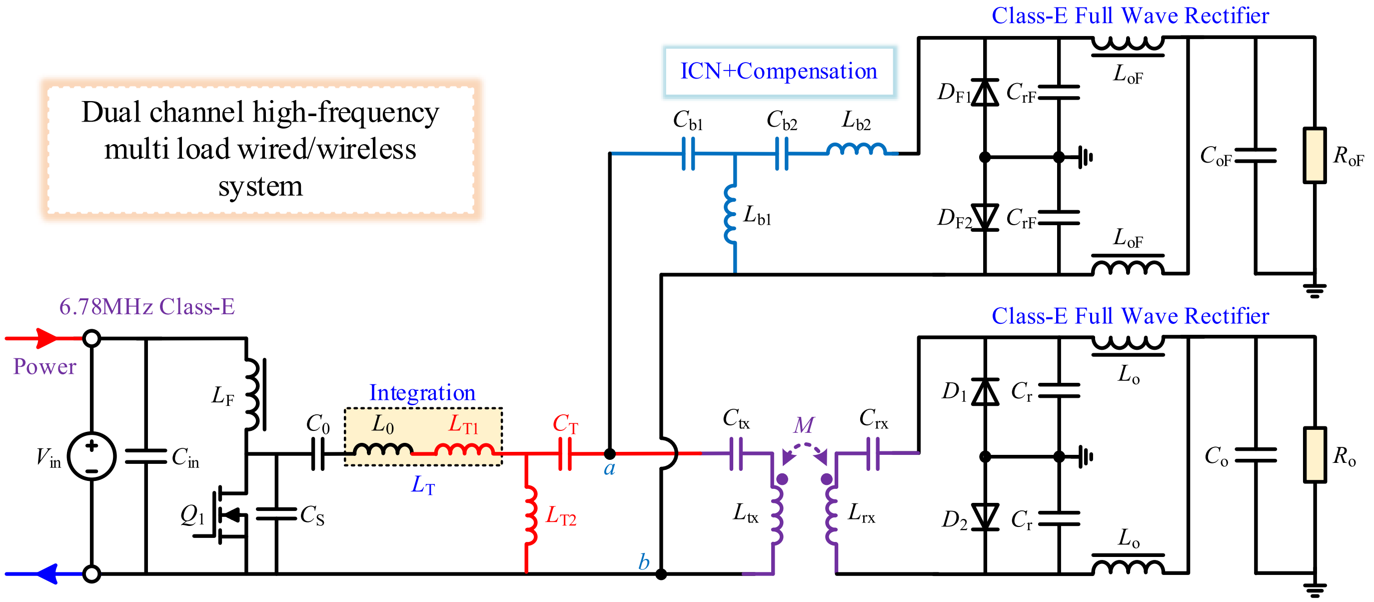

Fig. 18. 6.78 MHz wired/wireless dual-load high-frequency wireless power transfer system.

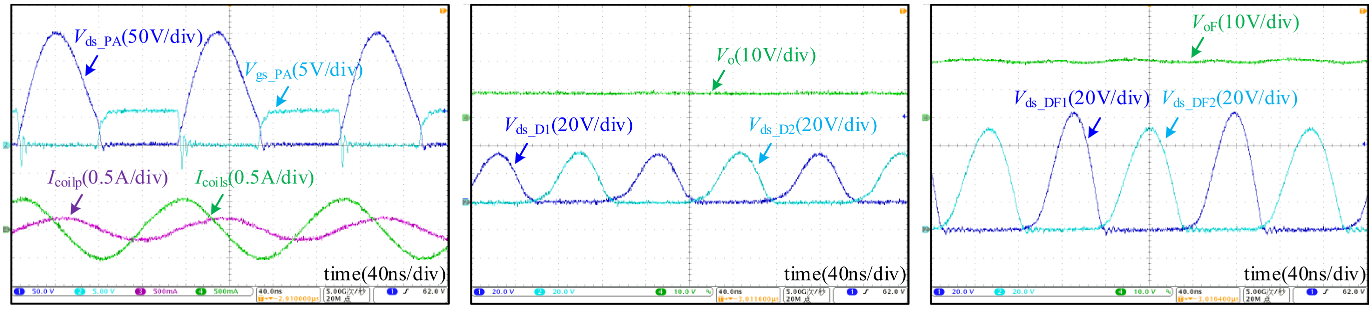

(a) (b) (c)

Fig. 19. When the mutual inductance is 1.796 uH, the power output is 33.87W. (a) PA and coil current. (b) Wireless branch rectification waveform and output voltage. (c) Wired branch rectification waveform and output voltage.

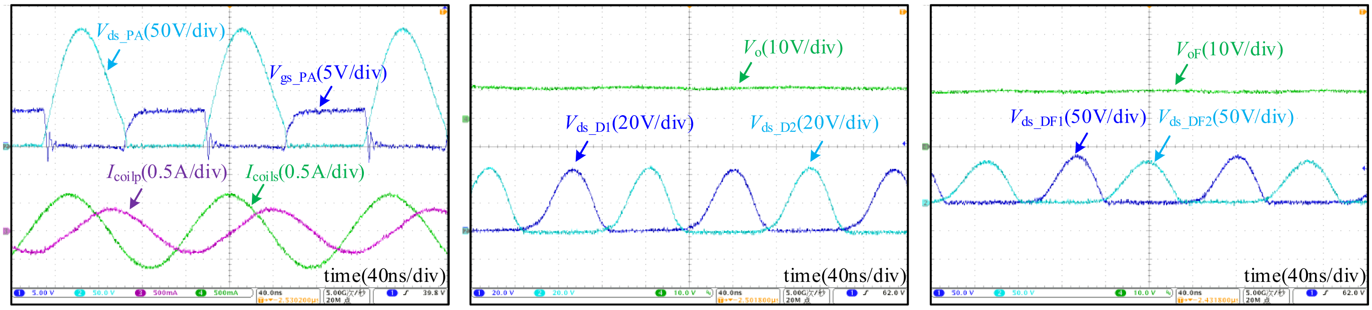

(a) (b) (c)

Fig. 20. When the mutual inductance is 1.48 uH, the power output is 36.28 W (a) PA and coil current. (b) Wireless branch rectification waveform and output voltage. (c) Wired branch rectification waveform and output voltage.

the overall efficiency of the system is 85.8% at this time. Fig. 20 corresponds to the situation where the system has an overall output of 36.28 W, and the overall efficiency of the system is 88.5% at this time. Fig. 21 corresponds to the situation where the system has an overall output of 40.93 W, and the overall efficiency of the system is 87.3% at this time. Such ideal efficiency maintenance is mainly due to the load compression principle that reduces the numerical variation range of the synthetic impedance

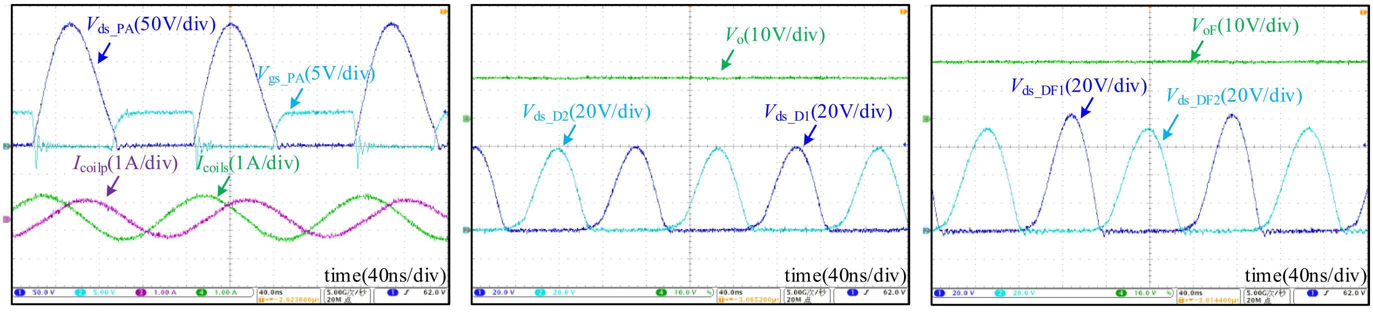

(a) (b) (c)

Fig. 21. When the mutual inductance is 1.157 uH, the power output is 40.93 W. (a) PA and coil current. (b) Wireless branch rectification waveform and output voltage. (c) Wired branch rectification waveform and output voltage.

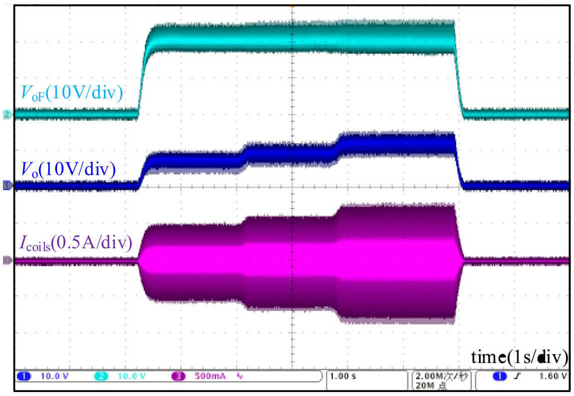

Fig. 22. System transient waveform when coupling coefficient changes.

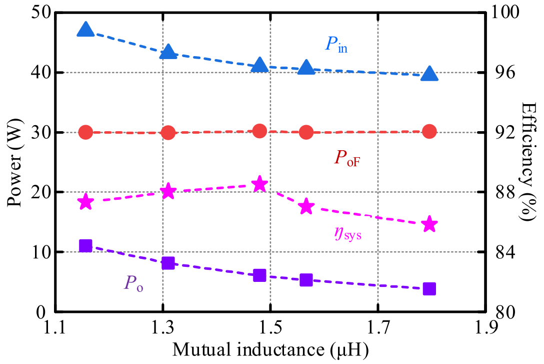

Fig. 23. System power and efficiency.

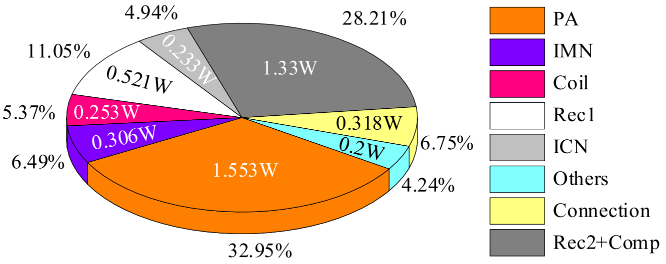

Fig. 24. The system loss distribution.

Z_{IMN}, thereby achieving high-efficiency operation of the PA. As shown in Figs. 19(a)–21(a), it can be seen that under different coil coupling conditions, the PA maintains a relatively good soft switching condition. Before the driving waveform reaches the threshold voltage of the gallium nitride switch, the drain-source voltage of the PA has almost dropped to 0 voltage. In addition, by observing the primary and secondary currents of the coil, it can be found that it exhibits a good sinusoidal characteristic, which means that the sinusoidal nature of the intermediate bus voltage is also relatively good. The secondary current leads the primary current by nearly 90 degrees, which also proves that the compensation network plays a corresponding role.

Fig. 22 shows the changes in the system's resonant state and external characteristics when the coupling coefficient suddenly decreases. It can be seen that as the position of the wireless branch changes suddenly twice, its output voltage increases accordingly, and the power also increases. The output voltage and power of the wired branch remain unchanged, which is consistent with the theoretical analysis. During the two abrupt change processes, it can be observed that there is no overshoot phenomenon in both the internal and external characteristics of the system, indicating that the system has good stability. In addition, due to the relatively low change in the current value of the switching tube and the small amplitude, the ON-resistance of the switching tube is also relatively stable, which further ensures the stable characteristics of the system. Fig. 23 shows the changes in the system's input and output power as well as the efficiency with the mutual inductance. Fig. 24 corresponds to the distribution of the system losses when the total output power is 36.28 W. The loss of ICN only accounts for about 0.776% of the output power of the wired branch, which has little impact on the gain of this branch. The losses are mainly concentrated in the traditional PA and the traditional rectifier part. Therefore, it is necessary to further propose a new type of high-efficiency low-voltage stress topology for replacement in the follow-up.

VI. DISCUSSION AND FUTURE RESEARCH

In real situations, fluctuations in the load are inevitable. Therefore, the impact of this situation on the system will be

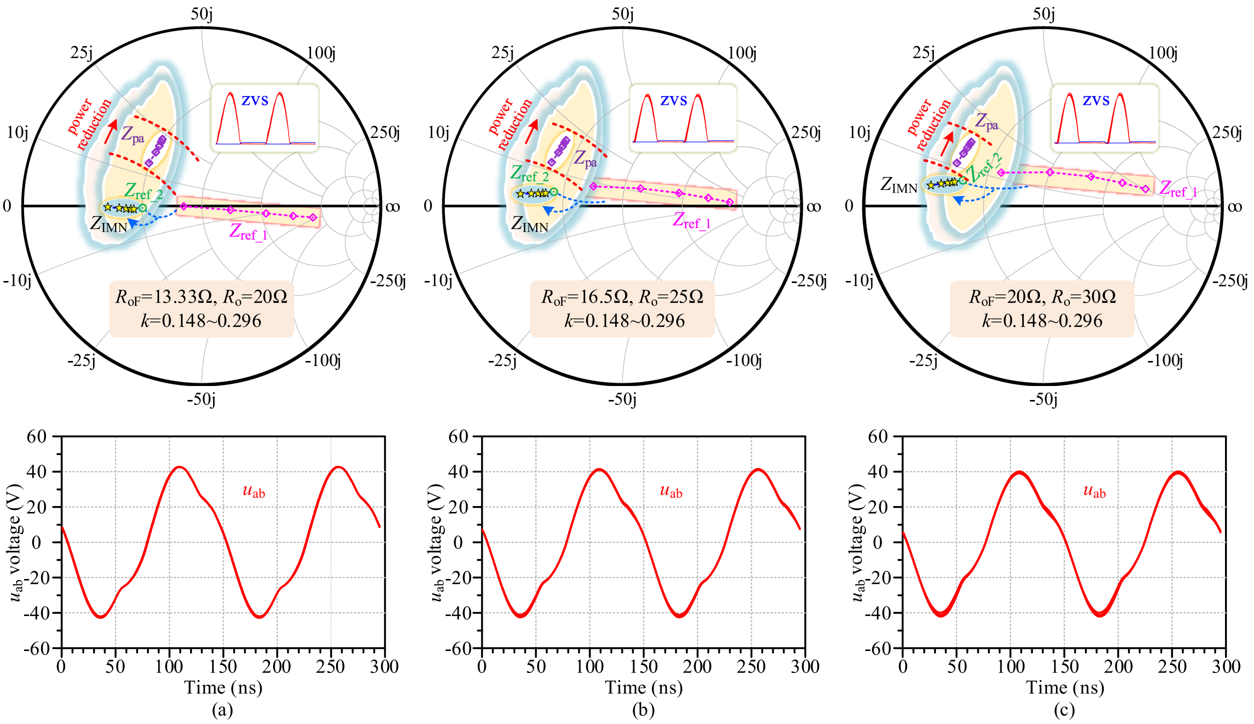

Fig. 25. Analysis of the system impedance trajectory and functional characteristics under the condition of load and coupling coefficient fluctuations for the dual-channel output. (a) R_{oF}=13.33 Ω, R_o=20 Ω. (b) R_{oF}=16.5 Ω, R_o=25 Ω, (c) R_{oF}=20 Ω, R_o=30 Ω.

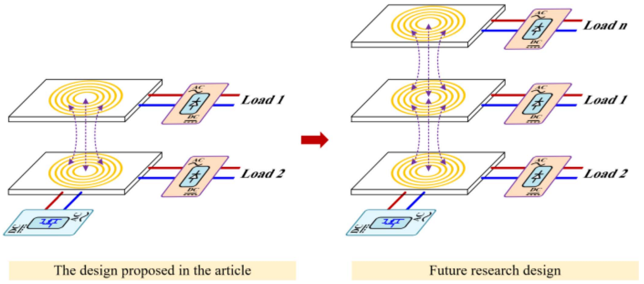

Fig. 26. High-frequency vertical power supply system.

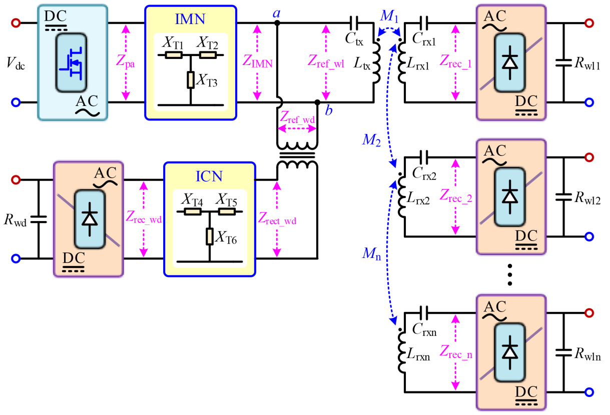

Fig. 27. Circuit structure of the vertical power supply system.

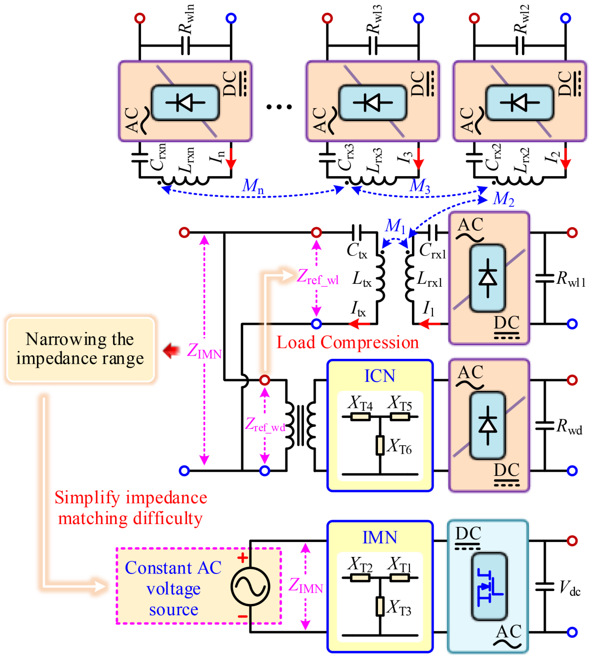

Fig. 28. Load impedance compression of the vertical power supply system.

discussed. Here, three cases are simulated and compared: R_{oF} = 13.33 Ω, R_o = 20 Ω; R_{oF} = 16.5 Ω, R_o = 25 Ω; and R_{oF} = 20Ω, R_o = 30 Ω. The changes in the impedance trajectory of the overall system and the impact on the functional output (u_{ab} and ZVS) are set to analyze, as shown in Fig. 25. It can be seen with the change of the load, the impedance values of the respective reflected impedances $Z_{\text{ref\_1}}$ and $Z_{\text{ref\_2}}$ have changed. However, the changing rule of the impedance trajectory

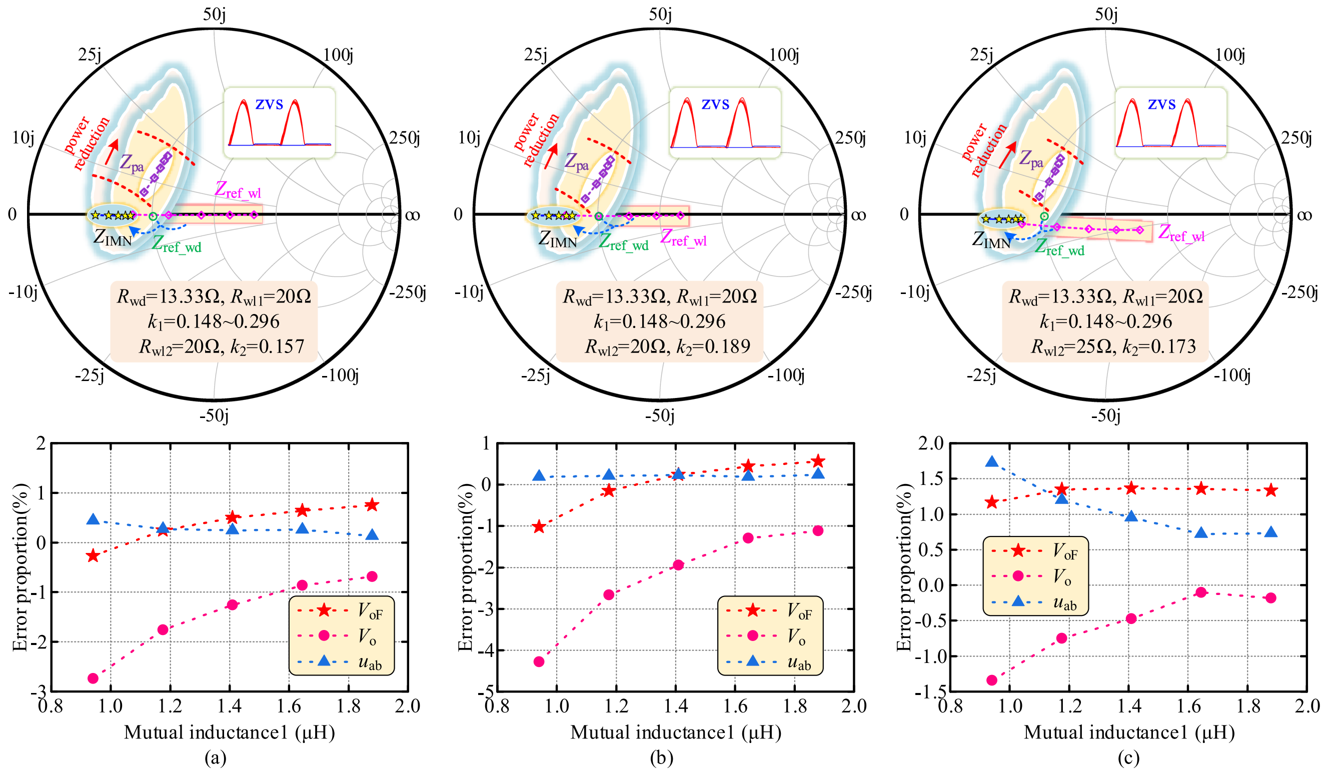

(a) (b) (c)

Fig. 29. Analysis of the system impedance trajectory and functional characteristics under the condition of load and coupling coefficient fluctuations for the multichannel output. (a) R_{wl2}=20 Ω, k_2=0.157. (b) R_{wl2}=20 Ω, k_2=0.189. (c) R_{wl2}=25 Ω, k_2=0.173.

is consistent, and the load impedance compression technology proposed in this article is still valid. The synthesized impedance Z_{IMN} has still been compressed. Z_{pa} is obtained through the same impedance matching network. Although the position of the impedance trajectory of Z_{pa} has changed, it is still within the high-efficiency operating range of the PA, and the ZVS is not affected. In addition, Fig. 25 shows the waveforms of the virtual voltage source u_{ab} under three different load conditions. It can be seen the load change has a very small impact on the amplitude of u_{ab}, so the circuit analysis of the subsequent system based on u_{ab} can basically be considered unaffected. In summary, the proposed design method can cope with the situation where the load and the coupling coefficient change simultaneously.

In the future, the number of loads of this system will be further expanded, and the core goal is to build a high-frequency vertical power supply system as shown in Fig. 26. To fully utilize the miniaturization and impedance characteristics of the high-frequency system, the high-frequency vertical power supply system will still be designed entirely using a 6.78 MHz circuit to maintain the integrated effect. Fig. 27 describes the circuit structure of the system, and the wired load branch will also be improved to an isolated design. By making full use of the unique impedance characteristics between each branch, a virtual busbar can be ingeniously constructed to simplify the design difficulty of the system, as shown in Fig. 28.

To verify the expandable characteristics of the vertical power supply system, simulations and analyses of the three-channel load output situation have been conducted, including one wired load and two wireless load situations, as shown in Fig. 29. The number of load branches has increased, changing from two to three. The coupling coefficient of wireless branch 1 has changed, and both the load and coupling coefficient of wireless branch 2 have changed. Here, the parameters of the wired branch and the wireless branch 1 are the same as those in the previous text. The rectification and compensation parameters of the wireless branch 2 are the same as those of the wireless branch 1. The load impedance compression technology proposed in this article can still be used. Z_{pa} is still within the high-efficiency impedance range of the PA, and ZVS can be achieved. In addition, the impact on the original wired branch and wireless branch 1 after adding the second wireless branch is specifically analyzed. The output voltage V_{oF} of the wired branch, the output voltage V_o of wireless branch 1, and the virtual voltage u_{ab} are selected as the analysis objects, and the error values of each variable after adding wireless branch 2 are calculated. The calculation is carried out by subtracting the original value from the value after adding wireless branch 2 and then dividing by the original value. Judging from the results in Fig. 29, the numerical deviation is very small, and the most severe case only fluctuates by 4.28%. That means, although a wireless branch has been added and both the load and coupling coefficient of this branch have changed, the impact on the previous two branches is minimal. This further illustrates that the technology proposed in this article can be applied to the situation where the load and coupling coefficient fluctuate simultaneously, and it also supports the extended application of more branches.

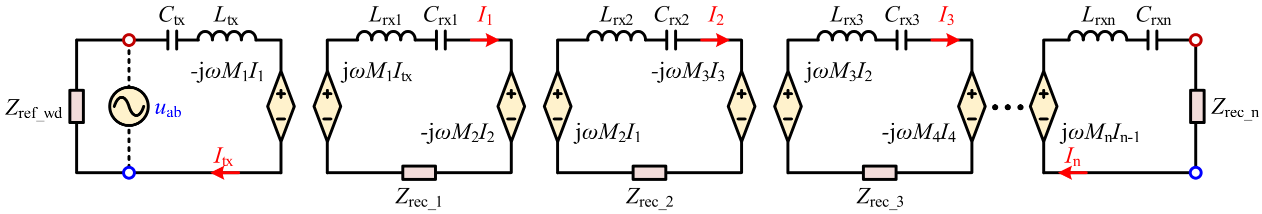

Fig. 30. Equivalent voltage source model of the vertical power supply system.

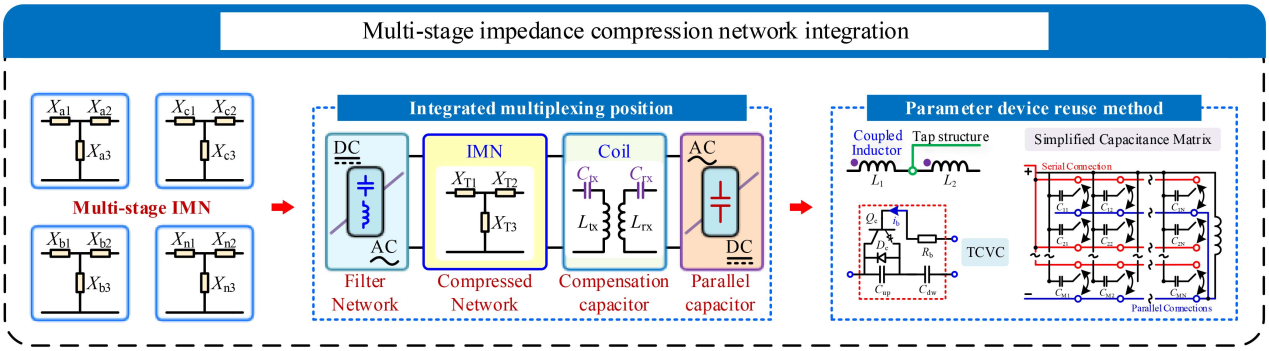

Fig. 31. Multiplexing and integration technology of segmented impedance compression network.

Furthermore, through the principle of the equivalent voltage source, combined with the selection of different rectifier types and functions, each branch can be endowed with a unique external characteristic output, as shown in Fig. 30. In addition, to support the hot-swappable function of the load, that is, the multimode selection of independent energy channel operation and the operation of any number of energy channels, it is necessary to further study the multiplexing and integration technology of the segmented impedance matching network. By integrating variable capacitors, capacitor matrices, coupled inductors, etc., a high-power density and low-complexity multimode IMN will be designed to meet the multimode operation requirements of the vertical power supply system, as shown in Fig. 31.

VII. CONCLUSION

In this article, an innovative design is developed for high-frequency wired/wireless dual-load applications. A load impedance compression principle and an intermediate voltage bus construction mechanism are proposed, which transforms the complex and mutually coupled multitrajectory model into a clear two-level system for solution. The feasibility of the theory is verified through experiments.

REFERENCES

[1] C. Cheng, W. Li, Z. Zhou, Z. Deng, and C. Mi, “A load-independent wireless power transfer system with multiple constant voltage outputs,” *IEEE Trans. Power Electron.*, vol. 35, no. 4, pp. 3328–3331, Apr. 2020, doi: 10.1109/TPEL.2019.2940091.

[2] C. Cheng, Z. Zhou, W. Li, Z. Deng, and C. C. Mi, “A power relay system with multiple loads using asymmetrical coil design,” *IEEE Trans. Ind. Electron.*, vol. 68, no. 2, pp. 1188–1196, Feb. 2021, doi: 10.1109/TIE.2020.2970636.

[3] C. Cheng et al., “A load-independent LCC-compensated wireless power transfer system for multiple loads with a compact coupler design,” *IEEE Trans. Ind. Electron.*, vol. 67, no. 6, pp. 4507–4515, Jun. 2020, doi: 10.1109/TIE.2019.2931260.

[4] Y. Zhang, T. Lu, Z. Zhao, F. He, K. Chen, and L. Yuan, “Employing load coils for multiple loads of resonant wireless power transfer,” *IEEE Trans. Power Electron.*, vol. 30, no. 11, pp. 6174–6181, Nov. 2015, doi: 10.1109/TPEL.2015.2396943.

[5] F. Liu, Y. Yang, Z. Ding, X. Chen, and R. M. Kennel, “A multifrequency superposition methodology to achieve high efficiency and targeted power distribution for a multiload MCR WPT system,” *IEEE Trans. Power Electron.*, vol. 33, no. 10, pp. 9005–9016, Oct. 2018, doi: 10.1109/TPEL.2017.2784566.

[6] X. Hou, Z. Wang, Y. Su, Z. Liu, and Z. Deng, “A dual-frequency dual-load multirelay magnetic coupling wireless power transfer system using shared power channel,” *IEEE Trans. Power Electron.*, vol. 37, no. 12, pp. 15717–15727, Dec. 2022, doi: 10.1109/TPEL.2022.3190143.

[7] D. Ahn and P. P. Mercier, “Wireless power transfer with concurrent 200-kHz and 6.78-MHz operation in a single-transmitter device,” *IEEE Trans. Power Electron.*, vol. 31, no. 7, pp. 5018–5029, Jul. 2016, doi: 10.1109/TPEL.2015.2480122.

[8] C. Zhao and D. Costinett, “GaN-based dual-mode wireless power transfer using multifrequency programmed pulse width modulation,” *IEEE Trans. Ind. Electron.*, vol. 64, no. 11, pp. 9165–9176, Nov. 2017, doi: 10.1109/TIE.2017.2681974.

[9] Y. Xiao, C. Liu, Y. Huang, and S. Liu, “Concurrent wireless power transfer to multiple receivers with additional resonant frequencies and reduced power switches,” *IEEE Trans. Ind. Electron.*, vol. 67, no. 11, pp. 9292–9301, Nov. 2020, doi: 10.1109/TIE.2019.2952787.

[10] L. Jiang and D. Costinett, “A high-efficiency GaN-based single-stage 6.78 MHz transmitter for wireless power transfer applications,” *IEEE Trans. Power Electron.*, vol. 34, no. 8, pp. 7677–7692, Aug. 2019, doi: 10.1109/TPEL.2018.2879958.

[11] M. Liu and M. Chen, “Dual-band wireless power transfer with reactance steering network and reconfigurable receivers,” *IEEE Trans. Power Electron.*, vol. 35, no. 1, pp. 496–507, Jan. 2020, doi: 10.1109/TPEL.2019.2913991.

[12] X. Zhang, F. Liu, and T. Mei, “Multifrequency phase-shifted control for multiphase multiload MCR WPT system to achieve targeted power distribution and high misalignment tolerance,” *IEEE Trans. Power Electron.*, vol. 36, no. 1, pp. 991–1003, Jan. 2021, doi: 10.1109/TPEL.2020.3000511.

[13] R. Narayanamoorthi, A. Vimala Juliet, and B. Chokkalingam, "Cross interference minimization and simultaneous wireless power transfer to multiple frequency loads using frequency bifurcation approach," *IEEE Trans. Power Electron.*, vol. 34, no. 11, pp. 10898–10909, Nov. 2019, doi: 10.1109/TPEL.2019.2898453.

[14] H. Wang, C. Zhang, Y. Yang, H. W. R. Liang, and S. Y. R. Hui, "A comparative study on overall efficiency of two-dimensional wireless power transfer systems using rotational and directional methods," *IEEE Trans. Ind. Electron.*, vol. 69, no. 1, pp. 260–269, Jan. 2022, doi: 10.1109/TIE.2020.3048317.

[15] Y.-J. Kim, D. Ha, W. J. Chappell, and P. P. Irazoqui, "Selective wireless power transfer for smart power distribution in a miniature-sized multiple-receiver system," *IEEE Trans. Ind. Electron.*, vol. 63, no. 3, pp. 1853–1862, Mar. 2016, doi: 10.1109/TIE.2015.2493142.

[16] E. S. Lee, J. S. Choi, H. S. Son, S. H. Han, and C. T. Rim, "Six degrees of freedom wide-range ubiquitous IPT for IoT by DQ magnetic field," *IEEE Trans. Power Electron.*, vol. 32, no. 11, pp. 8258–8276, Nov. 2017, doi: 10.1109/TPEL.2017.2691063.

[17] S. Li, X. Yu, Y. Yuan, S. Lu, and T. Li, "A novel high-voltage power supply with MHz WPT techniques: Achieving high-efficiency, high-isolation, and high-power-density," *IEEE Trans. Power Electron.*, vol. 38, no. 12, pp. 14794–14805, Dec. 2023, doi: 10.1109/TPEL.2023.3305054.

[18] Y. Wang, Z. Sun, Y. Guan, and D. Xu, "Overview of megahertz wireless power transfer," *Proc. IEEE*, vol. 111, no. 5, pp. 528–554, May 2023, doi: 10.1109/JPROC.2023.3265689.

[19] Z. Sun, Y. Wang, J. Sun, Y. Guan, and D. Xu, "Design of a strong robust wireless power transfer system with wide-range output regulation based on dual-band architecture," *IEEE Trans. Ind. Electron.*, vol. 70, no. 11, pp. 11142–11152, Nov. 2023, doi: 10.1109/TIE.2022.3225824.

[20] Z. Sun, Y. Chi, Y. Wang, Y. Guan, and D. Xu, "Analysis and design of a high frequency wireless battery charging system with smooth mode transition characteristics," *IEEE Trans. Power Electron.*, vol. 38, no. 11, pp. 13273–13285, Nov. 2023, doi: 10.1109/TPEL.2023.3300924.

[21] M. Liu, M. Fu, and C. Ma, "Parameter design for a 6.78-MHz wireless power transfer system based on analytical derivation of class E current-driven rectifier," *IEEE Trans. Power Electron.*, vol. 31, no. 6, pp. 4280–4291, Jun. 2016, doi: 10.1109/TPEL.2015.2472565.

[22] M. Liu, M. Fu, and C. Ma, "Low-harmonic-contents and high-efficiency class E full-wave current-driven rectifier for megahertz wireless power transfer systems," *IEEE Trans. Power Electron.*, vol. 32, no. 2, pp. 1198–1209, Feb. 2017, doi: 10.1109/TPEL.2016.2551288.

[23] Y. Shao, N. Kang, H. Zhang, R. Ma, M. Liu, and C. Ma, "A lightweight and robust drone MHz WPT system via novel coil design and impedance matching," *IEEE Trans. Ind. Appl.*, vol. 59, no. 3, pp. 3851–3864, May/Jun. 2023, doi: 10.1109/TIA.2023.3249146.

[24] Y. Shao, H. Zhang, M. Liu, and C. Ma, "Explicit design of impedance matching networks for robust MHz WPT systems with different features," *IEEE Trans. Power Electron.*, vol. 37, no. 9, pp. 11382–11393, Sep. 2022, doi: 10.1109/TPEL.2022.3165296.

[25] J. Song, M. Liu, and C. Ma, "Analysis and design of a high-efficiency 6.78-MHz wireless power transfer system with scalable number of receivers," *IEEE Trans. Ind. Electron.*, vol. 67, no. 10, pp. 8281–8291, Oct. 2020, doi: 10.1109/TIE.2019.2950850.

[26] M. Fu, T. Zhang, X. Zhu, P. C.-K. Luk, and C. Ma, "Compensation of cross coupling in multiple-receiver wireless power transfer systems," *IEEE Trans. Ind. Informat.*, vol. 12, no. 2, pp. 474–482, Apr. 2016, doi: 10.1109/TII.2016.2516906.

[27] H. Yin, M. Fu, M. Liu, J. Song, and C. Ma, "Autonomous power control in a reconfigurable 6.78-MHz multiple-receiver wireless charging system," *IEEE Trans. Ind. Electron.*, vol. 65, no. 8, pp. 6177–6187, Aug. 2018, doi: 10.1109/TIE.2017.2784338.

[28] M. Fu, H. Yin, and C. Ma, "Megahertz multiple-receiver wireless power transfer systems with power flow management and maximum efficiency point tracking," *IEEE Trans. Microw. Theory Techn.*, vol. 65, no. 11, pp. 4285–4293, Nov. 2017, doi: 10.1109/TMTT.2017.2689747.

[29] M. Fu, H. Yin, M. Liu, Y. Wang, and C. Ma, "A 6.78 MHz multiple-receiver wireless power transfer system with constant output voltage and optimum efficiency," *IEEE Trans. Power Electron.*, vol. 33, no. 6, pp. 5330–5340, Jun. 2018, doi: 10.1109/TPEL.2017.2726349.

[30] M. Liu, M. Fu, Y. Wang, and C. Ma, "Battery cell equalization via megahertz multiple-receiver wireless power transfer," *IEEE Trans. Power Electron.*, vol. 33, no. 5, pp. 4135–4144, May 2018, doi: 10.1109/TPEL.2017.2713407.

[31] Y. Guan, Y. Wang, W. Wang, and D. Xu, "Analysis and design of a high-frequency DC/DC converter based on a resonant rectifier," *IEEE Trans. Ind. Electron.*, vol. 64, no. 11, pp. 8492–8503, Nov. 2017, doi: 10.1109/TIE.2017.2698412.

[32] Y. Guan, C. Liu, Y. Wang, W. Wang, and D. Xu, "Analytical derivation and design of 20-MHz DC–DC soft-switching resonant converter," *IEEE Trans. Ind. Electron.*, vol. 68, no. 1, pp. 210–221, Jan. 2021, doi: 10.1109/TIE.2020.2965508.

[33] K. Jin, L. Gu, and J. Wang, "A 10-MHz resonant converter with a synchronous rectifier for low-voltage applications," *IEEE Trans. Power Electron.*, vol. 34, no. 4, pp. 3339–3347, Apr. 2019, doi: 10.1109/TPEL.2018.2850300.

[34] T. Huang, Y. Chen, B. Zhang, and D. Qiu, "Shared external driver for VHF converter with a synchronous rectifier based on matching network parameters optimization," *IEEE Trans. Ind. Electron.*, vol. 71, no. 2, pp. 1481–1491, Feb. 2024, doi: 10.1109/TIE.2023.3262892.

[35] Y. Guan, Z. Shi, C. Liu, Y. Wang, and D. Xu, "A 10 MHz DC/DC converter with zero-phase difference synchronous driving signal," *IEEE Trans. Power Electron.*, vol. 36, no. 12, pp. 13878–13888, Dec. 2021, doi: 10.1109/TPEL.2021.3084975.

[36] H. Thanh Le, Y. Nour, A. Han, F. Jensen, Z. Ouyang, and A. Knott, "Microfabricated air-core toroidal inductor in very high-frequency power converters," *IEEE J. Emerg. Sel. Top. Power Electron.*, vol. 6, no. 2, pp. 604–613, Jun. 2018, doi: 10.1109/JESTPE.2018.2798927.

[37] D. Zhang et al., "Optimal duty ratio assisted PFM control for VHF isolated class E DC-DC converter," *IEEE Trans. Power Electron.*, vol. 38, no. 12, pp. 15467–15480, Dec. 2023, doi: 10.1109/TPEL.2023.3317910.

[38] Y. Guan, C. Liu, Y. Wang, W. Wang, and D. Xu, "Analysis and design of a high-frequency low-profile converter for bendable equipment," *IEEE Trans. Power Electron.*, vol. 36, no. 11, pp. 12834–12842, Nov. 2021, doi: 10.1109/TPEL.2021.3078749.

[39] N. Weitz, S. Utzelmann, S. Ditze, and M. März, "A resonant push–pull DC–DC converter with an intrinsic current source behavior for radio frequency power conversion," *IEEE Trans. Power Electron.*, vol. 37, no. 6, pp. 7001–7012, Jun. 2022, doi: 10.1109/TPEL.2022.3142431.

[40] B. Li and K. Ngo, "An improved class-E current inverter with two coupled inductors for isolation and power scaling without affecting switch voltage stress," *IEEE Trans. Ind. Electron.*, vol. 71, no. 8, pp. 9947–9950, Aug. 2024, doi: 10.1109/TIE.2023.3319748.

[41] L. Zhao et al., "An integrated 6.78-MHz class $\Phi 2$ converter using bifurcation phenomenon of resonance between the isolation transformer," *IEEE Trans. Power Electron.*, vol. 39, no. 10, pp. 12003–12007, Oct. 2024, doi: 10.1109/TPEL.2024.3423715.

[42] Z. Zhang, K. Xu, Z.-W. Xu, J. Xu, X. Ren, and Q. Chen, "GaN VHF converters with integrated air-core transformers," *IEEE Trans. Power Electron.*, vol. 34, no. 4, pp. 3504–3515, Apr. 2019, doi: 10.1109/TPEL.2018.2849063.

[43] J. Feng, Q. Li, F. C. Lee, and M. Fu, "LCCL-LC resonant converter and its soft switching realization for omnidirectional wireless power transfer systems," *IEEE Trans. Power Electron.*, vol. 36, no. 4, pp. 3828–3839, Apr. 2021, doi: 10.1109/TPEL.2020.3024757.

[44] J. Tian and A. P. Hu, "A DC-voltage-controlled variable capacitor for stabilizing the ZVS frequency of a resonant converter for wireless power transfer," *IEEE Trans. Power Electron.*, vol. 32, no. 3, pp. 2312–2318, Mar. 2017, doi: 10.1109/TPEL.2016.2559798.

[45] Y. Lim, H. Tang, S. Lim, and J. Park, "An adaptive impedance-matching network based on a novel capacitor matrix for wireless power transfer," *IEEE Trans. Power Electron.*, vol. 29, no. 8, pp. 4403–4413, Aug. 2014, doi: 10.1109/TPEL.2013.2292596.

[46] S. Sinha, A. Kumar, B. Regensburger, and K. K. Afridi, "Active variable reactance rectifier—A new approach to compensating for coupling variations in wireless power transfer systems," *IEEE J. Emerg. Sel. Top. Power Electron.*, vol. 8, no. 3, pp. 2022–2040, Sep. 2020, doi: 10.1109/JESTPE.2019.2958894.

[47] S. Liu, M. Liu, S. Han, X. Zhu, and C. Ma, "Tunable class E^2 DC–DC converter with high efficiency and stable output power for 6.78-MHz wireless power transfer," *IEEE Trans. Power Electron.*, vol. 33, no. 8, pp. 6877–6886, Aug. 2018, doi: 10.1109/TPEL.2017.2762924.

Zhan Sun (Student Member, IEEE) was born in Heilongjiang Province, China, in 1997. He received the B.S. and M.S. degrees in electrical engineering in 2019 and 2021, respectively, from Harbin Institute of Technology, Harbin, China, where he is currently working toward the Ph.D. degree in electrical engineering.

His research interests include wireless power transfer, magnetic coupling structure design, high frequency, and very high frequency converters.

Yijie Wang (Senior Member, IEEE) was born in Heilongjiang Province, China, in 1982. He received the B.S., M.S., and Ph.D. degrees in electrical engineering from Harbin Institute of Technology, Harbin, China, in 2005, 2007, and 2012, respectively.

From 2012 to 2014, he was a Lecturer with the Department of Electrical and Electronics Engineering, Harbin Institute of Technology. From 2014 to 2017, he was an Associate Professor with the Department of Electrical and Electronics Engineering, Harbin Institute of Technology. Since 2017, he has been a Professor with the Department of Electrical and Electronics Engineering, Harbin Institute of Technology. His research interests include dc–dc converters, soft-switching power converters, power factor correction circuits, digital control electronic ballasts, and LED lighting systems.

Dr. Wang is an Associate Editor for IEEE TRANSACTIONS ON INDUSTRIAL ELECTRONICS, IEEE JOURNAL OF EMERGING AND SELECTED TOPICS IN POWER ELECTRONICS, IEEE ACCESS, *IET Power Electronics*, and *Journal of Power Electronics.*

Xianrui Zeng was born in Guangxi, China, in 1997. He received the B.S. degree in electrical engineering and the M.S. degree in academic discipline: electrical engineering and automation from the Harbin Institute of Technology, Harbin, China, in 2020 and 2022, respectively.

He is currently a Research Engineer with the Institute of Spacecraft System Engineering, China Academy of Space Technology. His research focuses on wireless power and data transmission systems, magnetic coupling optimization for aerospace applications, with particular emphasis on high-efficiency energy transfer solutions for spacecraft systems.

Yueshi Guan (Senior Member, IEEE) was born in Heilongjiang, China, in 1990. He received the B.S., M.S., and Ph.D. degrees in electrical engineering from the Harbin Institute of Technology (HIT), Harbin, China, in 2013, 2015, and 2019, respectively.

Since 2019, he has been an Associate Professor with the Department of Electrical and Electronics Engineering, HIT. His research interests are in the areas of high-frequency and very high-frequency converters, single-stage ac/dc converter, and light-emitting diode lighting systems.

Dianguo Xu (Fellow, IEEE) received the B.S. degree in control engineering from Harbin Engineering University, Harbin, China, in 1982, and the M.S. and Ph.D. degrees in electrical engineering from Harbin Institute of Technology (HIT), Harbin, China, in 1984 and 1989, respectively.

In 1984, he was with the Department of Electrical Engineering, HIT, as an Assistant Professor. Since 1994, he has been a Professor with the Department of Electrical Engineering, HIT. He was the Dean of School of Electrical Engineering and Automation, HIT, from 2000 to 2010. He was the Vice President of HIT, from 2014 to 2020. He has authored or coauthored more than 600 technical papers. His research interests include renewable energy generation technology, power quality mitigation, sensorless vector controlled motor drives, and high performance servo system.

Dr. Xu is the Chairman of IEEE Harbin Section, Co-EIC of IEEE TRANSACTIONS ON POWER ELECTRONICS, an Associate Editor for IEEE TRANSACTIONS ON INDUSTRIAL ELECTRONICS, IEEE JOURNAL OF EMERGING AND SELECTED TOPICS IN POWER ELECTRONICS. He was the recipient of the 2018 IEEE IAS Outstanding Achievement Award.